AD_____

Award Number: W81XWH-06-1-0431

TITLE: Optimization of Tomosynthesis Imaging for Improved Mass and Microcalcification Detection in the Breast

PRINCIPAL INVESTIGATOR: Dan Xia

CONTRACTING ORGANIZATION: The University of Chicago
Chicago, IL, 60637

REPORT DATE: April 2007

TYPE OF REPORT: Annual Summary

PREPARED FOR: U.S. Army Medical Research and Materiel Command
Fort Detrick, Maryland 21702-5012

DISTRIBUTION STATEMENT: Approved for Public Release;
Distribution Unlimited

The views, opinions and/or findings contained in this report are those of the author(s) and should not be construed as an official Department of the Army position, policy or decision unless so designated by other documentation.

REPORT DOCUMENTATION PAGE

Form Approved
OMB No. 0704-0188

Public reporting burden for this collection of information is estimated to average 1 hour per response, including the time for reviewing instructions, searching existing data sources, gathering and maintaining the data needed, and completing and reviewing this collection of information. Send comments regarding this burden estimate or any other aspect of this collection of information, including suggestions for reducing this burden to Department of Defense, Washington Headquarters Services, Directorate for Information Operations and Reports (0704-0188), 1215 Jefferson Davis Highway, Suite 1204, Arlington, VA 22202-4302. Respondents should be aware that notwithstanding any other provision of law, no person shall be subject to any penalty for failing to comply with a collection of information if it does not display a currently valid OMB control number. **PLEASE DO NOT RETURN YOUR FORM TO THE ABOVE ADDRESS.**

1. REPORT DATE	2. REPORT TYPE	3. DATES COVERED
01-04-2007	Annual Summary	15 Mar 2006 – 14 Mar 2007

4. TITLE AND SUBTITLE

Optimization of Tomosynthesis Imaging for Improved Mass and Microcalcification Detection in the Breast

5a. CONTRACT NUMBER

5b. GRANT NUMBER
W81XWH-06-1-0431

5c. PROGRAM ELEMENT NUMBER

5d. PROJECT NUMBER

5e. TASK NUMBER

5f. WORK UNIT NUMBER

6. AUTHOR(S)

Dan Xia

Email: DANXIA@UCHICAGO.EDU

7. PERFORMING ORGANIZATION NAME(S) AND ADDRESS(ES)

The University of Chicago
Chicago, IL, 60637

8. PERFORMING ORGANIZATION REPORT NUMBER

9. SPONSORING / MONITORING AGENCY NAME(S) AND ADDRESS(ES)
U.S. Army Medical Research and Materiel Command
Fort Detrick, Maryland 21702-5012

10. SPONSOR/MONITOR'S ACRONYM(S)

11. SPONSOR/MONITOR'S REPORT NUMBER(S)

12. DISTRIBUTION / AVAILABILITY STATEMENT
Approved for Public Release; Distribution Unlimited

13. SUPPLEMENTARY NOTES

14. ABSTRACT
Although considerable progress has been made for the breast tomosynthesis, there are still some issues should be addressed before it becomes suitable for routine clinical use: (1) development of accurate and efficient algorithms for reconstructing 3D breast images from tomosynthesis data, (2) the effect of various physical factors on image quality. During the first year of this research, we have implemented and investigated the TV-based algorithm for image reconstruction in breast tomosynthesis, and investigated the convergence property of the TV-based algorithm under different data conditions and different constraint parameters. We have also conducted numerical studies to investigate the image reconstruction by use of the TV-based algorithm and the existing EM and ART algorithms for different imaging configurations in breast tomosynthesis. Furthermore, we have investigated some physical factors such as cone-beam data noise and non-isotropic spatial resolution on tomosynthesis images.

15. SUBJECT TERMS
tomosynthesis, iterative algorithms, convergence, scanning configuration, physical factors

16. SECURITY CLASSIFICATION OF:			17. LIMITATION OF ABSTRACT	18. NUMBER OF PAGES	19a. NAME OF RESPONSIBLE PERSON
a. REPORT	b. ABSTRACT	c. THIS PAGE			USAMRMC
U	U	U	UU	38	19b. TELEPHONE NUMBER *(include area code)*

Table of Contents

Page

Introduction…….…….….. **4**

Body…….. **5**

Key Research Accomplishments…….. **7**

Reportable Outcomes…… **8**

Conclusion…… **9**

References…… **10**

Appendices…… **11**

INTRODUCTION

Breast tomosynthesis is a tomographic imaging technique, and it has the potential advantage to overcome a major limitation of conventional mammography through recovering, to a large degree, the loss of 3D information about the breast in conventional, 2D mammography. In the last several years, there has been renewed interest in developing breast tomosynthesis for detection of breast cancer [1,2]. Although considerable progress has been made, improvements to several areas of breast tomosynthesis technology are still needed before it becomes suitable for routine clinical use. In essence, breast tomosynthesis can be considered as a dedicated computed tomography with limited view for breast imaging, and it thus requires the development of special reconstruction algorithms for recovering 3D breast images from tomosynthesis data. In addition, various physical factors in breast tomosynthesis can strongly affect the resulting image quality, and the issue of patient radiation dose in breast tomosynthesis is of a concern. The overall objective of this project is to investigate and develop reconstruction algorithms for obtaining breast images of practical use, to investigate and evaluate systematically the effects of various physical factors on image quality in breast tomosynthesis, and to use and evaluate (empirical) techniques for effectively compensating for the effects on breast tomosynthesis images and for possibly reducing imaging radiation dose in breast tomosynthesis. It is fully expected that the research will contribute to the effort in the field to develop and improve breast tomosynthesis for its clinical use. This report summarizes the progress of this Predoctoral Traineeship Award project made by the recipient during the past one year.

BODY

1 Training Accomplishments

At the time of this report, the recipient, Dan Xia, of the Predoctoral Traineeship Award has taken 22 out of 22 required courses towards his Ph.D. degree in medical physics. The courses include physics of medical imaging, physics of radiation therapy, mathematics for medical physicists, image processing, statistics, anatomy of the body, radiation biology and teaching assistant training.

2 Research Accomplishments

2.1 Investigation of reconstruction algorithms for breast tomosynthesis

In tomosynthesis, data are acquired only at a small number of projection views over a limited angular range. Therefore, tomosynthesis data are highly sparse as compared to data acquired in conventional computed tomography (CT). Consequently, existing analytical algorithms for accurate reconstruction of CT images are generally not suitable for yielding useful images from tomosynthesis data. For example, the effect of filtering may not completely be canceled out due to the limited number of views and limited angular range, resulting in prominent artifacts in reconstructed images. In contrast, iterative algorithms can generally produce images with less artifacts than can the analytic algorithms. In the project, we are investigating and developing a total variation (TV) based iterative algorithm for reconstructing accurate images from incomplete projection data [3]. We have investigated the following issues: (1) Performance of the TV-based algorithm when applied to tomosynthesis data generated from discrete images. In this case, one has a discrete matrix system, which allows ideal reconstructions of the underlying discrete images. The result in this study provides the upper bound on the performance of the TV-based and any other reconstruction algorithm. (2) Convergence conditions of the TV-based algorithm under different data conditions and different constraint parameters. This investigation is critical for any iterative algorithm to be practically useful. We have successfully addressed issue (1) and are working actively on issue (2).

2.2 Investigation of scanning configurations in breast tomosynthesis

Currently, breast tomosynthesis acquires data at about 12 to 20 projection views over a limited angular range around 20 to 50 degrees. Typically, a circular source trajectory is adopted for collection of cone-beam projections. It remains, however, largely unexplored as to what the optimal scanning configurations are. In the last several months, we have conducted initial investigation on image reconstruction from data acquired (1) at a small number of views and (2) over a limited angular range. In the studies, data were collected from different phantoms, including a breast phantom developed in Ref. [4], at different numbers of views.

We first generated cone-beam data at 15, 20, 40, and 60 projection views over 2π. The reason for the angular range is 2π is that the study results would not be affected by the issue of the limited angular range. From these data sets, we have used the TV-based algorithm to reconstruct images. For comparison, we have also conducted preliminary reconstructions by using the expectation-maximization (EM) algorithm and the algebraic reconstruction

technique (ART). Although we are currently in the process of analyzing these reconstruction results, the initial evaluation appears to indicate that the TV-based algorithm is more accurate than the EM and ART algorithms in reconstructing images from few-view data.

We subsequently studied image reconstruction from data acquired over a limited angular range. Specifically, we have selected angular ranges of $\pi/4$, $\pi/2$, and π and collected data at 15, 20, 40, and 60 views over each of these angular ranges. From the collected data, we reconstructed images by use of the TV-based algorithm. For comparison, the EM and ART algorithms were also used for reconstructing images from these data sets. Our initial analysis of these results suggests [5] that (1) when the angular range decreases, image quality obtained with these algorithms decreases, and (2) the TV-based algorithm generally yields images with less artifacts than do the EM and ART algorithms. We are still in the process of conducting additional studies on this problem.

2.3 Investigation of the physical factors in tomosynthesis imaging

Various physical factors can significantly affect image quality in breast tomosynthesis. These factors include data noise, non-uniform image spatial resolution, scatter, and detector responses. We have begun to perform research on investigating and correcting for the effect of physical factors on image quality. In our preliminary studies, we have evaluated the effects of two physical factors, (1) cone-beam data noise and (2) non-uniform image resolution.

In an attempt to separate the issues of few-view and limited angular range from data noise, we have first performed a thorough noise study for image reconstruction from projection data collected at a large number of views over 2π. The result of this study will provide a theoretical guidance to the investigation of the noise properties in tomosynthesis in which data are acquired at a small number of views over a limited angular range. In this study, we specifically focus on investigating how data noise are propagated into the reconstructed images. Both analytic and numerical analyses were carried out, and the results indicate that variances of reconstructed images are spatially varying and that the levels of variances in different regions are not affecting significantly each other [6]. Because the study was based upon analytic result, it was computationally possible to accomplish this initial study. On the other hand, noise studies involve the iterative algorithms such as the TV-based, EM, and ART algorithms are much more demanding computationally. We have just begun to perform the image noise studies by using the iterative algorithms.

In current breast tomosynthesis, the spatial resolution within a transverse plane is much finer than that along the longitudinal direction, and image representation with non-isotropic spatial resolution is used in iterative algorithms for reducing computational time. Such an image representation can lead to significant artifacts in iterative reconstruction. In the last couple of months, we have been investigating the effect of non-isotropic image representation on iterative reconstruction accuracy of breast tomosynthesis images. We have reconstructed images by use of TV-based, EM, and ART algorithms for image representations with different ratios of the in-plane and longitudinal resolution. Our results demonstrate that non-isotropic image representation can lead to significant artifacts in reconstructed images. The appearance and severity of the artifacts depend not only upon the ratio between the in-plane and longitudinal resolution but also upon the iterative algorithms. The TV-based algorithm seems to be less susceptible to the effect than the EM and ART algorithms. Through the selection of algorithm parameters, the artifacts can be reduced [7].

KEY RESEARCH ACCOMPLISHMENTS

- We have implemented the modification to the TV-based algorithm tailored to breast tomosynthesis.
- We have also implemented and tested the EM and ART algorithms.
- We have conducted an investigation of the upper bound on the performance of TV-based algorithm for image reconstruction from tomosynthesis data.
- We have conducted a preliminary investigation of the convergence property of the TV-based algorithm under different data conditions and different constraint parameters in reconstruction of tomosynthesis images.
- We have carried out preliminary investigations of the scanning configurations in breast tomosynthesis imaging by using different numbers of views over different angular ranges.
- We have performed a preliminary study on the effect of some physical factors on breast tomosynthesis. The physical factors were considered in the study include data noise and non-isotropic spatial resolution.

REPORTABLE OUTCOMES

Peer-reviewed Journal Articles

1. **D. Xia**, L. Yu, E. Y. Sidky, Y. Zou, N. Zuo, and X. Pan: Noise properties of chord-image reconstruction, IEEE Trans. Med. Imaging, (in press), 2007.

Conference Proceeding Articles

1. **D. Xia**, E. Y. Sidky, L. Yu, and X. Pan: Noise properties in helical cone-beam CT images, Proc. MIC, M14-420, 2006.

Conference Presentations and Abstracts

1. **D. Xia**, E. Sidky, J. Bian, I. Reisner, R. Nishikawa, and X. Pan: Image representation with non-isotropic spatial resolution on iterative reconstruction accuracy in breast tomosynthesis, submitted to RSNA annual meeting, 2007.
2. **D. Xia**, J. Bian, I. Reisner, E. Sidky, R. Nishikawa, and X. Pan: Investigation of scanning and reconstruction approach for tomosynthesis breast imaging, submitted to AAPM annual meeting, 2007.
3. **D. Xia**, E. Y. Sidky, L. Yu, and X. Pan: Noise properties in helical cone-beam CT images, presented at IEEE Medical Image Conference, 2006.

Honors and Awards

- Student traveling award, IEEE Medical Imaging Conference, 2006
- Student Travel Contingency Grant, SPIE Medical Imaging Conference, 2007

CONCLUSIONS

The recipient of the Predoctoral Traineeship Award has finished the required courses towards his Ph.D. degree. These trainings have proven useful for the recipient to achieve the proposed research goals.

During the first year, we have implemented and investigated the TV-based algorithm for image reconstruction in breast tomosynthesis. We first evaluated the performance of the algorithm under ideal conditions and its convergence properties. We have subsequently conducted numerical studies to investigate the image reconstruction by use of the TV-based algorithm and the existing EM and ART algorithms for different imaging configurations in breast tomosynthesis. Our results suggest that, in general, the TV-based algorithm provide tomosynthesis images with quality higher than EM and ART algorithms in terms of the metrics such as root-mean-square error and image resolution. Furthermore, we have investigated the effect of some physical factors, such as data noise and non-isotropic spatial resolution, on tomosynthesis images. Overall, we have achieved the goals for the first year and laid down the foundation for the research in the next two years. Our aims in the next two years include, based upon what we have learned from the results described above, further investigating and streamlining the TV-based algorithm in terms of convergence, speed, and rubostness. Careful, comparative evaluation studies of reconstruction algorithms will be conducted under more realistic physical conditions. In particular, we will expand our data-generation programs to include non-linear partial volume, beam-hardening, and scatter effects in our data. We will implement existing algorithms to correct for the scatter effect before image reconstruction. Additionally, we will generalize reconstruction algorithms, including the TV-based, EM, and ART algorithms to incorporate these factors so that they can be compensated for during reconstruction iterations. We will look into the results from current studies in other groups in our department on the effect of detector response, which is expect to be spatially varying, on data acquisition. If it is significant, we will include the detector response into the data-generation program and reconstruction algorithms. We will also perform tomosynthesis experiments to collect real data of physical breast phantoms for additional evaluation of the scanning configurations and reconstruction algorithms. Finally, we will select real-patient data for testing and assessing the reconstruction algorithm.

REFERENCES

1. J. T. Dobbins III and D. J. Godfrey: Digital x-ray tomosynthesis: current state of the art and clinical potential, Phys. Med. Biol., **48**, R65-R106, 2003.

2. M. Bissonnette, M. Hansroul, E. Masson, S. Savard, S. Cadieux, P. Warmoes, D. Gravel, J. Agopyan, B. Polischuk, W. Haerer, T. Mertelmeier, J. Y. Lo, Y. Chen, J. T. Dobbins III, J. L. Jesneck, and S. Singh: Digital breast tomosynthesis using an amorphous selenium flat panel detector, Proc. SPIE, **5745**, pp. 529, 2005.

3. E. Sidky, C.-M. Kao, and X. Pan: Accurate image reconstruction from few-views and limited-angle data in divergent-beam CT, J. X-ray Sci. Tech. **14,** pp. 119-139, 2006.

4. I. Reiser, E. Sidky, R. Nishikawa, and X. Pan: Development of an analytic breast phantom for quantitative comparaison of reconstruction algorithms for digital breast tomosynthesis, Proceedings of 8th international workshop, IWDM, pp. 190-196, 2006.

5. D. Xia, J. Bian, I. Reisner, E. Sidky, R. Nishikawa, and X. Pan: Investigation of scanning and reconstruction approach for tomosynthesis breast imaging, submitted to AAPM annual meeting, 2007.

6. D. Xia, L. Yu, E. Y. Sidky, Y. Zou, N. Zuo, and X. Pan: Noise properties of chord-image reconstruction, IEEE Trans. Med. Imaging, (in press), 2007.

7. D. Xia, E. Sidky, J. Bian, I. Reisner, R. Nishikawa, and X. Pan: Image representation with non-isotropic spatial resolution on iterative reconstruction accuracy in breast tomosynthesis, submitted to RSNA annual meeting, 2007.

APPENDICES

- Appendix A: **D. Xia**, E. Sidky, J. Bian, I. Reisner, R. Nishikawa, and X. Pan: Image representation with non-isotropic spatial resolution on iterative reconstruction accuracy in breast tomosynthesis, submitted to RSNA annual meeting, 2007.
- Appendix B: **D. Xia**, J. Bian, I. Reisner, E. Sidky, R. Nishikawa, and X. Pan: Investigation of scanning and reconstruction approach for tomosynthesis breast imaging, submitted to AAPM annual meeting, 2007.
- Appendix C: **D. Xia**, L. Yu, E. Y. Sidky, Y. Zou, N. Zuo, and X. Pan: Noise properties of chord-image reconstruction, IEEE Trans. Med. Imaging, (in press), 2007.

Image representation with non-isotropic spatial resolution on iterative reconstruction accuracy in breast tomosynthesis

Dan Xia, Emil Sidky, Junguo Bian, Ingrid Reiser, Robert Nishikawa, Xiaochuan Pan

Department of Radiology, The University of Chicago
5841 S Maryland Avenue, Chicago, IL 60637

Clinical Relevance/Application:
Breast tomosynthesis has received renewed interest because it can provide 3D information about the breast. This work concerns iterative reconstruction of accurate breast tomosynthesis images.

Purpose:
In current breast tomosynthesis, image representation with non-isotropic spatial resolution is used for reducing computational time. This can, however, lead to artifacts in iterative reconstruction of breast tomosynthesis images. In the work, we investigate the effect of non-isotropic image representation on the reconstruction accuracy. Based upon the investigation, we devise schemes for reducing artifacts in iterative reconstruction.

Materials and Method:
In the work, we focus on investigating the effect of non-isotropic image representation on reconstruction accuracy of iterative algorithms. The iterative algorithms under study include the total-variation (TV) based, expectation maximization (EM), and algebraic reconstruction technique (ART) algorithms. Tomosynthesis data are generated at 12 and 20 views over 50 degrees from phantoms, including a breast phantom. We have reconstructed images by using image representations with different degrees of non-isotropic spatial resolution. Specifically, in each image representation, the ratio between the in-plane and longitudinal resolution for an image voxel is selected to be a value less than 1.

Results:
We have reconstructed images by use of TV-based, EM, and ART algorithms for image representations with different ratios of in-plane and longitudinal resolution. Our results demonstrate that non-isotropic image representation can lead to significant artifacts in reconstructed images. The appearance and severity of the artifacts depend not only upon the ratio between the in-plane and longitudinal resolution but also upon the iterative algorithms. The TV-based algorithm seems to be less susceptible to the effect than the EM and ART algorithms. Through the selection of algorithm parameters, the artifacts can be reduced.

Conclusion:
The non-isotropic image representation can significantly affect reconstruction accuracy obtained with iterative algorithms in breast tomosynthesis.

Investigation of scanning and reconstruction approach for tomosynthesis breast imaging

D. Xia, J. Bian, I. Reisner, E. Sidky, R. Nishikawa, X. Pan

Department of Radiology, The University of Chicago
5841 S Maryland Avenue, Chicago, IL 60637

Purpose:
Investigation and application of scanning and reconstruction approaches to tomosynthesis breast imaging.

Materials and Method:
Tomographic imaging such as tomosynthesis has the advantages to overcome the major limitation of conventional mammography. The loss of information in 2D projection imaging can be recovered in tomographic imaging. In tomosynthesis, the acquired data are highly sparse as compared to CT data. Therefore, image reconstruction in tomosynthesis is challenging. Moreover, it remains largely unexplored as to what the optimal scanning configurations are. Recently, we have developed a TV-based iterative algorithm for accurate images from sparse or incomplete projection data. In this work, we will investigate image reconstruction by use of the TV-based algorithm. Moreover, using this algorithm and other algorithms, we investigate the optimal scanning geometries in tomosynthesis breast imaging. Specifically, we have investigated scanning configurations in terms of number of projection views and the range of scanning angle.

Results:
We have conducted numerical studies to investigate image reconstruction and scanning parameters by use of the TV-based algorithm and other algorithms. From numerical and physical phantom, we have acquired projection data from physical phantoms for different scanning configurations. From these data sets, we reconstruct images by using the TV-based algorithm. For comparison, other algorithms, including the FBP algorithm. Using various evaluation indices, we characterize the reconstructed image quality and, from which, we evaluate the performance of the reconstruction algorithms and scanning configurations.

Conclusion:
In this work, we have investigated different scanning configurations and reconstruction algorithms, including the TV-based algorithm, in tomosynthesis breast imaging. Both computer-simulation data and real physical phantom data were used. Our results suggest that, in general, the TV-based algorithm can provide higher image quality for tomosynthesis imaging than other algorithms and that increasing the scanning angular range can considerably improve image quality.

Noise Properties of Chord-image Reconstruction

Dan Xia[1], Lifeng Yu[1], Emil Y. Sidky[1], Yu Zou[1], Nianming Zuo[2], and Xiaochuan Pan[1,*]
[1]Department of Radiology, The University of Chicago, USA
[2]National Laboratory of Pattern Recognition, Institute of Automation,
Chinese Academy of Sciences
[*]Corresponding author

Abstract

Recently, there has been much progress in algorithm development for image reconstruction in cone-beam computed tomography (CT). Current algorithms, including the chord-based algorithms, now accept minimal data sets for obtaining images on volume regions-of-interest (ROIs) thereby potentially allowing for reduction of x-ray dose in diagnostic CT. As these developments are relatively new, little effort has been directed at investigating the response of the resulting algorithm implementations to physical factors such as data noise. In this work, we perform an investigation on the noise properties of ROI images reconstructed by using chord-based algorithms for different scanning configurations. We find that, for the cases under study, the chord-based algorithms yield images with comparable quality. Additionally, it is observed that, in many situations, large data sets contain extraneous data that may not reduce the ROI-image variances.

Key Words: CT, Cone-beam CT, Reconstruction, Chord, Noise

1 Introduction

In recent years, exact algorithms have been developed for reconstructing images [1] and for reconstructing images on "π-lines" [2, 3, 4] from helical cone-beam data. Since 2005, works have being published on algorithm development for reconstructing images on chords for general trajectories [5, 6, 7, 8]. Some of these algorithms can reconstruct images within three dimensional (3D) regions of interest (ROIs) from cone-beam data containing both longitudinal and transverse truncations. The introduction of the M-line concept and reconstruction [5, 9] provides additional flexibility for covering volume ROIs.

As these algorithm developments are relatively recent, little effort has been directed at investigating their noise properties. With the algorithm development for ROI-image reconstruction, it has been tacitly assumed that the reduction in necessary scanning angle and in projection data may lead to ROI images from less radiation exposure. This conclusion may, however, depend on the noise properties of reconstruction algorithms. If ROI reconstruction from the minimal (or reduced) data set leads to noisier ROI images than reconstruction of the same ROI from a larger data set, it may be necessary to increase the x-ray source intensity for the ROI-data set to attain the same image quality as those reconstructed from larger data sets. Such an increase can offset the fact that reduced or minimum projection data are needed for ROI reconstruction.

The focus of this work is to investigate the noise properties of image reconstruction from minimal data set and large data sets by use of chord-based algorithms. We demonstrate that the minimal data set can indeed lead to actual reduction of radiation exposure for attaining comparable image quality, defined in terms of image variance, as that obtained with a larger data set. In Sec. 2, we briefly summarize the chord-based reconstruction algorithms: backprojection filtration (BPF) [2, 6], minimum data filtered backprojection (MDFBP) [4, 6], and filtered backprojection (FBP) [6, 10] algorithms. In Sec. 3, we perform analysis and empirical studies on noise

properties of images reconstructed from parallel-beam fan-beam, and cone-beam data. Finally, discussion is given in Sec. 4.

2 Chord-based Reconstruction Algorithms

We consider a continuous source trajectory specified by $\vec{r}_0(s) = (x(s),\, y(s),\, z(s))$, where $x(s)$, $y(s)$, and $z(s)$ denote the x-, y-, and z-components of $\vec{r}_0(s)$ in the fixed-coordinate system, and s is a curve parameter indicating the position of the x-ray source on the trajectory. The projection data of the object function $f(\vec{r})$ can be mathematically expressed as

$$D(\vec{r}_0(s), \hat{\beta}) \quad = \quad \int_0^\infty dt\, f(\vec{r}_0(s) + t\,\hat{\beta}), \tag{1}$$

where the unit vector $\hat{\beta}$ denotes the direction of a specific x-ray passing through the point $\vec{r}$. We also introduce two additional coordinate systems $\{u, v, w\}$ and $\{u_d, v_d\}$ to describe the geometry in a general scan. They are fixed on the rotating source point and the cone-beam projection of the source point, respectively, which are referred to as the rotation-coordinate and detector-coordinate systems. Let $\hat{\mathrm{e}}_u(s)$, $\hat{\mathrm{e}}_v(s)$, and $\hat{\mathrm{e}}_w(s)$ denote the orthogonal unit vectors of the rotation-coordinate system. The rotation-coordinate system can be chosen such that $\hat{\mathrm{e}}_u(s)$ and $\hat{\mathrm{e}}_w(s)$ are within the x-y plane and $\hat{\mathrm{e}}_v(s)$ is parallel to the z-axis. One can also choose the "well oriented" coordinate system as the rotation-coordinate system [5], in which unit vector $\hat{\mathrm{e}}_u(s)$ is parallel to and unit vectors $\hat{\mathrm{e}}_v(s)$ and $\hat{\mathrm{e}}_w(s)$ are perpendicular to the direction of $\frac{d\vec{r}_0(s)}{ds}$. We assume that a detector plane is placed at a distance S from the source point and orients along $\hat{\mathrm{e}}_w(s)$. The detector-coordinate system $\{u_d, v_d\}$ is the cone-beam projection of the 2D-coordinate system $\{u, v\}$ onto the detector plane, and the u_d- and v_d-axis are along $\hat{\mathrm{e}}_u(s)$ and $\hat{\mathrm{e}}_v(s)$, respectively. In this situation, we also use $P(u_d, v_d, s)$ to denote the cone-beam projection, thus $D(\vec{r}_0(s), \hat{\beta}) = P(u_d, v_d, s)$, when

$$\hat{\beta} = \frac{1}{A(u_d, v_d)}\,[u_d\,\hat{\mathrm{e}}_u(s) + v_d\,\hat{\mathrm{e}}_v(s) - S\,\hat{\mathrm{e}}_w(s)] \quad \text{and} \quad A(u_d, v_d) = \sqrt{u_d^2 + v_d^2 + S^2}. \tag{2}$$

In a 2D case, it can be observed that $v_d = 0$. For notational convenience, we use $A(u_d)$ and $P(u_d, s)$ to denote $A(u_d, 0)$ and $P(u_d, 0, s)$, respectively.

A chord is a line segment connecting two points $\vec{r}_0(s_a)$ and $\vec{r}_0(s_b)$ on the trajectory. Any point $\vec{r}$ on the chord can be expressed as

$$\vec{r} = \frac{\vec{r}_0(s_a) + \vec{r}_0(s_b)}{2} + x_c\,\hat{\mathrm{e}}_c, \qquad x_c \in [-l, l], \tag{3}$$

where $\hat{\mathrm{e}}_c = \frac{\vec{r}_0(s_b) - \vec{r}_0(s_a)}{|\vec{r}_0(s_b) - \vec{r}_0(s_a)|}$ denotes the direction of the chord, and $l = \frac{1}{2}\,|\vec{r}_0(s_b) - \vec{r}_0(s_a)|$ is one half of the chord length. For a helical trajectory, the curve parameter s is linearly related to the rotation angle λ, and in the current work, we select $s = \lambda$. When s_a and s_b are within one turn, the chord becomes the conventional π-line segment [2, 11, 12]. The intersection between a chord and the object is referred as a *support segment*. Let x_{c1} and x_{c2} represent the end points of a support segment. Because the trajectory under consideration never intersects the object, we have $[x_{c1}, x_{c2}] \subset [-l, l]$. Therefore, one can use (x_c, s_a, s_b) and $f_c(x_c, s_a, s_b)$ to denote a point and the corresponding image on the chord. We have previously developed three algorithms, which are referred to as the BPF [2, 6, 10], MDFBP [4, 6], and FBP [6, 10] algorithms, respectively, for exact image reconstruction on a chord of a general trajectory.

2.1 The BPF algorithm

The BPF algorithm [2, 6] reconstructs the image on a chord specified by s_a and s_b as

$$f_c(x_c, s_a, s_b) = \hat{f}(x_c, s_a, s_b) + \frac{1}{2\pi}\frac{P(u_{d0}, v_{d0}, s_a)}{b(x_c)}\left[\frac{\sqrt{(l-x_B)(l-x_A)}}{l-x_c} + \frac{\sqrt{(l+x_A)(l+x_B)}}{l+x_c}\right], \quad (4)$$

where $x_c \in [x_A, x_B]$, and parameters x_A and x_B are two points on the chord satisfying $[x_{c1}, x_{c2}] \subseteq [x_A, x_B] \subset [-l, l]$. The function $b(x_c)$ is defined as $b(x_c) = \sqrt{(x_B - x_c)(x_c - x_A)}$, and $P(u_{d0}, v_{d0}, s_a)$ denotes the projection along the chord specified by s_a and s_b. The filtered image $\hat{f}(x_c, s_a, s_b)$ is given by

$$\hat{f}(x_c, s_a, s_b) = \frac{1}{2\pi^2}\frac{1}{b(x_c)}\int_{\mathbf{R}} \frac{dx'_c}{x_c - x'_c}\, b(x'_c)\, g(x'_c, s_a, s_b), \quad (5)$$

where the backprojection image on the chord can be written as

$$\begin{aligned} g(x'_c, s_a, s_b) &= \Pi_c(x'_c)\int_{s_a}^{s_b} ds\, \frac{\mathrm{sgn}(-\hat{\beta}\cdot\hat{\mathrm{e}}_w)}{|\vec{r}\,' - \vec{r}_0(s)|^2}\left\{-\frac{d\vec{r}_0(s)}{ds}\cdot\hat{\beta}\, P(u_d, v_d, s)\right. \\ &+ \left[\frac{d\vec{r}_0(s)}{ds}\cdot\hat{\mathrm{e}}_u(s) + \frac{u_d}{S(s)}\frac{d\vec{r}_0(s)}{ds}\cdot\hat{\mathrm{e}}_w(s)\right] A(u_d, v_d)\frac{\partial P(u_d, v_d, s)}{\partial u_d} \\ &+ \left.\left[\frac{d\vec{r}_0(s)}{ds}\cdot\hat{\mathrm{e}}_v(s) + \frac{v_d}{S(s)}\frac{d\vec{r}_0(s)}{ds}\cdot\hat{\mathrm{e}}_w(s)\right] A(u_d, v_d)\frac{\partial P(u_d, v_d, s)}{\partial v_d}\right\}, \end{aligned} \quad (6)$$

and the rect function $\Pi_c(x'_c)$=1 if $x'_c \in [x_A, x_B]$ and 0 otherwise. It can be observed in Eq. (4) that the chord image can be obtained exactly from knowledge of the backprojection image $g(x'_c, s_a, s_b)$ for $x'_c \in [x_A, x_B]$, which we refer to as the *reconstruction segment* because it determines the actual reconstruction interval on the chord. In particular, because the reconstruction segment $[x_A, x_B]$ can be chosen as small as the support segment $[x_{c1}, x_{c2}]$, the chord image can be reconstructed from knowledge of $g(x'_c, s_a, s_b)$ only on the support segment. This interesting property of the Hilbert transform forms the basis for exact image reconstruction on a chord from projections containing longitudinal or transverse truncations [13].

2.2 The MDFBP algorithm

The BPF algorithm reconstructs the chord image by performing a 1D filtration (i.e., the integration over x'_c in Eq. (4)) of the backprojection image (i.e., the integration over s in Eq. (6)). On the other hand, the MDFBP algorithm [4, 6] reconstructs the chord image by performing a 1D data filtration (i.e., the integration over u'_c) prior to their backprojection (i.e., the integration over s) onto the chord:

$$\begin{aligned} f_c(x_c, s_a, s_b) &= \frac{1}{2\pi^2}\frac{1}{b(x_c)}\int_{s_a}^{s_b} ds[w_2(1-u_c) + w_1 u_c]\int_{\mathbb{R}} \frac{du'_c}{u_c - u'_c} P_\Pi \\ &+ \frac{1}{2\pi}\frac{P(u_{d0}, v_{d0}, s_a)}{b(x_c)}\left[\frac{\sqrt{(l-x_B)(l-x_A)}}{l-x_c} + \frac{\sqrt{(l+x_A)(l+x_B)}}{l+x_c}\right], \end{aligned} \quad (7)$$

where the modified data function is given by

$$\begin{aligned} P_\Pi &= \Pi_c(x'_c)\frac{b(x'_c)}{w_2(1-u'_c) + w_1 u'_c}\frac{\mathrm{sgn}(-\hat{\beta}\cdot\hat{\mathrm{e}}_w)}{|\vec{r}\,' - \vec{r}_0(s)|^2}\left\{-\frac{d\vec{r}_0(s)}{ds}\cdot\hat{\beta}\, P(u_d, v_d, s)\right. \\ &+ \left[\frac{d\vec{r}_0(s)}{ds}\cdot\hat{\mathrm{e}}_u(s) + \frac{u_d}{S(s)}\frac{d\vec{r}_0(s)}{ds}\cdot\hat{\mathrm{e}}_w(s)\right] A(u_d, v_d)\frac{\partial P(u_d, v_d, s)}{\partial u_d} \\ &+ \left.\left[\frac{d\vec{r}_0(s)}{ds}\cdot\hat{\mathrm{e}}_v(s) + \frac{v_d}{S(s)}\frac{d\vec{r}_0(s)}{ds}\cdot\hat{\mathrm{e}}_w(s)\right] A(u_d, v_d)\frac{\partial P(u_d, v_d, s)}{\partial v_d}\right\}, \end{aligned}$$

$w_1 = -[\vec{r}_0(s_a) - \vec{r}_0(s)] \cdot \hat{e}_w$, and $w_2 = -[\vec{r}_0(s_b) - \vec{r}_0(s)] \cdot \hat{e}_w$. For a source position s, the variables u_c and u'_c denote the cone-beam projections of x_c and x'_c onto the detector and can be obtained, respectively, by replacing x with x_c and x'_c in

$$u = \frac{w_2(x+l)}{w_1(l-x) + w_2(x+l)}. \tag{8}$$

The rect function $\Pi_c(x'_c)$ in Eq. (8) indicates that the MDFBP algorithm can reconstruct a chord image from knowledge of data only on the cone-beam projection of the reconstruction segment $[x_A, x_B]$, which can be as small as the support segment. Therefore, similar to the BPF algorithm, the MDFBP algorithm can also reconstruct a chord image from data containing truncations [4, 6].

2.3 The FBP algorithm

The chord-based FBP algorithm [6, 10] can be expressed as

$$f_c(x_c, s_a, s_b) = \frac{1}{2\pi^2} \int_{s_a}^{s_b} ds \frac{A}{|\vec{r} - \vec{r}_0(s)|} \int_{-\infty}^{\infty} \frac{du'_c}{u_c - u'_c} \frac{1}{|\vec{r}' - \vec{r}_0(s)|} \frac{\partial}{\partial q} D(\vec{r}_0(q), \hat{\beta}) \Big|_{q=s}, \tag{9}$$

where u_c indicates the cone-beam projection of x_c onto the detector and is determined by using x_c to replace x in Eq. (8), and A denotes the distance from the source point $\vec{r}_0(s)$ to a point on the detector at which the ray connecting $\vec{r}$ and $\vec{r}_0(s)$ intersects the detector. As the filtering (i.e., the integration over u'_c) is carried out over the projection of the straight line containing the chord, similar to other existing FBP-based algorithms, the chord-based FBP algorithm cannot exactly reconstruct ROI images from data containing transverse truncations.

2.4 Data-sufficiency conditions

As shown in Eq. (9), a data-sufficiency condition for the FBP algorithm is: (a) data are available over the trajectory segment $s \in [s_a, s_b]$, and (b) for each s, data on the cone-beam projection of the chord are non-truncated. This condition is similar to that for other FBP-based algorithms [1, 9, 14, 15, 16]. From Eqs. (4) and (7), a data-sufficiency condition for the chord-based BPF and MDFBP algorithms is: (a) data are collected over the trajectory segment $[s_a, s_b]$, and (b) at each s, data only on the cone-beam projection of the reconstruction segment $[x_A, x_B]$ on the chord are available. It follows that, because the reconstruction segment $[x_A, x_B]$ can be chosen as small as the support segment $[x_{c1}, x_{c2}]$, the BPF and MDFBP algorithms require, at each s, data only on the cone-beam projection of the support segment $[x_{c1}, x_{c2}]$ (instead of the entire chord-line as the chord-based FBP algorithm requires). Different selections of the reconstruction segment $[x_A, x_B]$ imply that different amounts of data at each s can be used for reconstructing the chord image. Under the ideal continuous conditions, different selections of $[x_A, x_B]$ yield identical chord images. However, when data contain noise and other inconsistencies, and when different selections of $[x_A, x_B]$ are used, the BPF and MDFBP algorithms in their discrete forms may yield different chord images. This is an issue that will be investigated below.

3 Noise Properties of Chord-based Image Reconstruction

The BPF, MDFBP, and FBP algorithms described above can be applied to reconstructing chord images from parallel-, fan-, and cone-beam data [17]. Algorithms analogous to the BPF algorithm that are capable of reconstructing 2D ROI images from truncation data have also previously been proposed [8, 13, 18]. We study below the noise properties of chord-based reconstruction by use of these algorithms in their discrete forms. As mentioned above, the BPF and MDFBP algorithms can reconstruct the image on the reconstruction segment $[x_A, x_B]$ as long as it covers the support segment $[x_{c1}, x_{c2}]$. We analyze image-noise properties on reconstruction segments of different lengths.

3.1 Analysis of image-noise properties

The chord-based algorithms invoke three major mathematical operations: differentiation, backprojection, and filtration. To a large extent, the BPF, MDFBP, and FBP algorithms differ in the orders of invoking these operations. Below, we focus on investigating the noise properties of differentiation, backprojection, and filtration in the BPF algorithm. The approach taken in the investigation is readily applicable to analyzing the noise properties of the MDFBP and FBP algorithms. In the presence of data noise, the measured projection $\mathbf{D}(\vec{r}_0(s), \hat{\beta})$ should be interpreted as a stochastic process. (Throughout the paper, we use boldface and normal letters to denote a stochastic process and its mean, respectively.) Because the backprojection $\mathbf{g}(x_c, s_a, s_b)$ and the final image $\mathbf{f}_c(x_c, s_a, s_b)$ on a chord are computed from $\mathbf{D}(\vec{r}_0(s), \hat{\beta})$, they should also be considered as stochastic processes. We focus in this section on investigating the chord-image variance $\mathbf{f}_c(x_c, s_a, s_b)$ by the investigation of noise propagation through each step involved in the BPF reconstruction algorithm.

3.1.1 Noise properties of the differentiation/backprojection for parallel-beam data

Let $\mathbf{P}(u_d, s)$ denote the parallel-beam projection on detector bin u_d acquired at view s. We assume the covariance of the projection data $\mathbf{P}(u_d, s)$ to be uncorrelated, i.e.,

$$\text{Cov}\{\mathbf{P}(u_d, s),\, \mathbf{P}(u'_d, s')\} = \sigma^2(u_d, s)\delta(u_d - u'_d)\delta(s - s'), \tag{10}$$

where $\sigma^2(u_d, s)$ denotes the variance of the projection data. The backprojection image on the chord is given by [13]

$$\mathbf{g}(x_c, s_a, s_b) = \int_{-\frac{\pi}{2}}^{\frac{\pi}{2}} ds\, \frac{\partial}{\partial u_d}\mathbf{P}(u_d, s), \tag{11}$$

where $u_d = \vec{r} \cdot \hat{\mathrm{e}}_u(s)$. The final image variances on a chord depend upon the covariance of the backprojection image, which, using Eq. (11), can be written as

$$\text{Cov}\{\mathbf{g}(x_c, s_a, s_b), \mathbf{g}(x'_c, s_a, s_b)\} = \int_{-\frac{\pi}{2}}^{\frac{\pi}{2}} ds \int_{-\frac{\pi}{2}}^{\frac{\pi}{2}} ds'\, \text{Cov}\{\frac{\partial}{\partial u_d}\mathbf{P}(u_d, s), \frac{\partial}{\partial u'_d}\mathbf{P}(u'_d, s')\}. \tag{12}$$

The evaluation of the backprojection-image covariance involves the data-derivative covariance, which can be conveniently written as

$$\text{Cov}\{\frac{\partial}{\partial u_d}\mathbf{P}(u_d, s), \frac{\partial}{\partial u'_d}\mathbf{P}(u'_d, s')\} = a\,\omega\,\sigma^2(u_d, s)\delta(u_d - u'_d)\delta(s - s') + \mathrm{T}_{para}(u_d, u'_d, s, s'), \tag{13}$$

where $\text{Var}\{\mathbf{P}(u_d, s)\} = \sigma^2(u_d, s)$ denotes the known data variance, which can be a function of u_d and s. The second term $\mathrm{T}_{para}(u_d, u'_d, s, s')$ represents the difference between the term on the left-hand side and the first term on the right-hand side of Eq. (13). Although the magnitude of $\mathrm{T}_{para}(u_d, u'_d, s, s')$ can be larger than or comparable to that of the first term in the right-hand side of Eq. (13), numerical results below show that its contribution to the final image variance on a chord is negligibly small. Therefore, we consider only the first term in the derivation of the chord-image variance below. The parameters a and ω are introduced to account for the interpolation effect of the discrete data derivative and discrete backprojection on the chord-image variance. Using the first term in Eq. (13), we can rewrite Eq. (12) as

$$\text{Cov}\{\mathbf{g}(x_c, s_a, s_b), \mathbf{g}(x'_c, s_a, s_b)\} \approx a\,\omega \int_{-\frac{\pi}{2}}^{\frac{\pi}{2}} ds\, \sigma^2(u_d, s)\delta(u_d - u'_d). \tag{14}$$

We now consider two points x_c and x'_c on the chord and let u_d and u'_d denote their parallel-beam or fan-beam

projections onto the detector. Clearly, for a source position s that satisfies $s \neq s_a$ or s_b, one can conclude that

$$\begin{aligned} u_d - u'_d &= 0 \quad \text{if} \quad x_c - x'_c = 0 \\ u_d - u'_d &\neq 0 \quad \text{if} \quad x_c - x'_c \neq 0. \end{aligned} \tag{15}$$

Thus, if $x_c = x'_c$, $\text{Cov}\{\mathbf{g}(x_c, s_a, s_b), \mathbf{g}(x_c, s_a, s_b)\} = \delta(0)\, a\, \omega \int_{-\frac{\pi}{2}}^{\frac{\pi}{2}} ds \sigma^2(u_d, s)$ and, if $x_c \neq x'_c$, $\text{Cov}\{\mathbf{g}(x_c, s_a, s_b), \mathbf{g}(x'_c, s_a, s_b)$ 0. Therefore, the covariance of the backprojection image for parallel-beam projections can be re-expressed as

$$\text{Cov}\{\mathbf{g}(x_c, s_a, s_b), \mathbf{g}(x'_c, s_a, s_b)\} \approx c(x_c)\, \delta(x_c - x'_c), \tag{16}$$

where

$$c(x_c) = a\omega \int_{-\frac{\pi}{2}}^{\frac{\pi}{2}} ds\, \sigma^2(u_d, s). \tag{17}$$

3.1.2 Noise properties of the differentiation/backprojection for fan-beam data

In the fan-beam case, we use $\mathbf{P}(u_d, s)$ to denote the projection on detector bin u_d acquired at view s. Again, we assume $\mathbf{P}(u_d, s)$ to be uncorrelated and satisfy Eq. (10). The backprojection image in Eq. (6) can be re-expressed as

$$\mathbf{g}(x_c, s_a, s_b) = \int_{s_a}^{s_b} ds\, \frac{1}{|\vec{r} - \vec{r}_0(s)|^2} \mathbf{P}'(u_d, s), \tag{18}$$

where $u_d = \frac{S\vec{r}\cdot\hat{\mathrm{e}}_u(s)}{(\vec{r}_0(s)-\vec{r})\cdot\hat{\mathrm{e}}_w(s)}$ is the fan-beam projection of x_c onto the detector. The weighted-data derivative $\mathbf{P}'(u_d, s)$ is given by

$$\mathbf{P}'(u_d, s) = A^2(u_d) \left| \frac{d\vec{r}_0(s)}{ds} \right| \frac{\partial}{\partial u_d} \left[\frac{\mathbf{P}(u_d, s)}{A(u_d)} \right]. \tag{19}$$

Using Eq. (18), one can write the covariance of the backprojection image as

$$\begin{aligned} \text{Cov}\{\mathbf{g}(x_c, s_a, s_b), \mathbf{g}(x'_c, s_a, s_b)\} &= \int_{s_a}^{s_b} ds \int_{s_a}^{s_b} ds' \, \frac{1}{|\vec{r} - \vec{r}_0(s)|^2} \frac{1}{|\vec{r} - \vec{r}_0(s')|^2} \\ &\times \quad \text{Cov}\{\mathbf{P}'(u_d, s), \mathbf{P}'(u'_d, s')\}, \end{aligned} \tag{20}$$

which depends upon the covariance of $\mathbf{P}'(u_d, s)$. Again, we can conveniently write the covariance of $\mathbf{P}'(u_d, s)$ as

$$\begin{aligned} \text{Cov}\{\mathbf{P}'(u_d, s), \mathbf{P}'(u'_d, s')\} &= a\, \omega\, \sigma^2(u_d, s)\, A^2(u_d) \left| \frac{d\vec{r}_0(s)}{ds} \right|^2 \delta(u_d - u'_d)\delta(s - s') \\ &+ \quad \mathrm{T}_{fan}(u_d, u'_d, s, s'), \end{aligned} \tag{21}$$

where $\text{Var}\{\mathbf{P}(u_d, s)\} = \sigma^2(u_d, s)$ denotes the known data variance, which can be a function of u_d and s. The second term $\mathrm{T}_{fan}(u_d, u'_d, s, s')$ represents the difference between the term on the left-hand side and the first term in the right-hand side of Eq. (21). As numerical results below indicate, it turns out that $\mathrm{T}_{fan}(u_d, u'_d, s, s')$ will also have a negligible contribution to the chord-image variance. Therefore, we consider only the first term in the derivation of the chord-image variance below. Again, the parameters a and ω are introduced to account for the interpolation effect of the discrete data derivative and discrete backprojection on the chord-image variance. Using the first term in Eq. (21), we can rewrite Eq. (20) as

$$\text{Cov}\{\mathbf{g}(x_c, s_a, s_b), \mathbf{g}(x'_c, s_a, s_b)\} \approx a\, \omega \int_{s_a}^{s_b} ds\, \frac{\sigma^2(u_d, s) A^2(u_d)}{|\vec{r} - \vec{r}_0(s)|^4} \left| \frac{d\vec{r}_0(s)}{ds} \right|^2 \delta(u_d - u'_d). \tag{22}$$

Similar to the parallel-beam case described above, using Eq. (15), one can conclude that

$$\text{Cov}\{\mathbf{g}(x_c, s_a, s_b), \mathbf{g}(x'_c, s_a, s_b)\} \approx c(x_c)\,\delta(x_c - x'_c), \tag{23}$$

where

$$c(x_c) = a\,\omega \int_{s_a}^{s_b} ds\, \frac{A^2(u_d)}{|\vec{r} - \vec{r}_0(s)|^4} \left| \frac{d\vec{r}_0(s)}{ds} \right|^2 \sigma^2(u_d, s). \tag{24}$$

3.1.3 Noise properties of the differentiation/backprojection for cone-beam data

In the cone-beam case, let $\mathbf{P}(u_d, v_d, s)$ denote the projection at view s on a detector bin specified by (u_d, v_d). In the so-called "well oriented" rotation-coordinate system [5], unit vector $\hat{\mathrm{e}}_u(s)$ is parallel to and unit vectors $\hat{\mathrm{e}}_v(s)$ and $\hat{\mathrm{e}}_w(s)$ are orthogonal, to the tangential direction $\frac{d\vec{r}_0(s)}{ds}$ of the source trajectory. Let u_d and v_d denote the coordinates along $\hat{\mathrm{e}}_u(s)$ and $\hat{\mathrm{e}}_v(s)$. It can be shown [5] that the backprojection image depends only upon the data derivative along u_d. Therefore, the reconstruction formula for the cone-beam backprojection image can be obtained from that for the fan-beam backprojection image in Eq. (18) by simply replacing $P(u_d, s)$ and $A(u_d)$ with $P(u_d, v_d, s)$ and $A(u_d, v_d)$, respectively, in Eq. (19). Subsequently, one can show that the covariance of the cone-beam backprojection image $\mathbf{g}(x_c, s_a, s_b)$ also satisfies Eqs. (23) and (24).

3.1.4 Estimation of parameters a and ω in discrete form

The parameter a is introduced to account for the interpolation effect of the discrete data-derivative on the chord-image variance. We consider a two-point derivative, which was used in our numerical studies. Let $\mathbf{P}_i$ denote the discrete data, where $i = 1, 2, ..., I$, and I indicates the total number of data points. We assume that data $\mathbf{P}_i$ are uncorrelated and use Var$\{\mathbf{P}_i\}$ to denote their variances. The two-point data derivative is defined as

$$\bar{\mathbf{P}}_i = \frac{1}{2}[\mathbf{P}_{i+1} - \mathbf{P}_{i-1}]. \tag{25}$$

Therefore, the variance of the discrete data derivative $\bar{\mathbf{P}}_i$ can be written as

$$\text{Var}\{\bar{\mathbf{P}}_i\} = \frac{1}{2}\frac{\text{Var}\{\mathbf{P}_{i+1}\} + \text{Var}\{\mathbf{P}_{i-1}\}}{2} \tag{26}$$

When data variances are identical, Eq. (26) becomes

$$\text{Var}\{\bar{\mathbf{P}}_i\} = \frac{1}{2}\text{Var}\{\mathbf{P}_i\}. \tag{27}$$

Therefore, in our studies, we select $a = \frac{1}{2}$, which is the coefficient in Eq. (27).

The parameter ω was introduced to account for the interpolation effect of discrete backprojection on the chord-image variances. The estimated value of ω depends obviously upon the specific interpolation scheme used in the discrete backprojection. We illustrate below our estimation of ω when a two-point interpolation is used for the discrete backprojection in the parallel- and fan-beam cases. One can readily obtain estimates of ω when other interpolation schemes are used. At a backprojection view s, we use $\mathbf{P}'_i$ to denote the discrete weighed-data derivatives. For a given u_d satisfying $i \leq u_d \leq (i+1)$, we express the interpolated weighted-data derivative as

$$\mathbf{P}'_{u_d} = (1-\gamma)\mathbf{P}'_i + \gamma\mathbf{P}'_{i+1}, \tag{28}$$

where $\gamma = u_d - i$. Furthermore, we can write the variance of $\mathbf{P}'_{u_d}$ as

$$\text{Var}\{\mathbf{P}'_{u_d}\} \approx [(1-\gamma)^2 + \gamma^2]\text{Var}\{\mathbf{P}'_i\} \tag{29}$$

For the seek of simplifying the estimation of ω, we have ignored the correlation between $\mathbf{P}'_i$ and $\mathbf{P}'_{i+1}$ and assumed that $\text{Var}\{\mathbf{P}'_i\} \approx \text{Var}\{\mathbf{P}'_{i+1}\}$. We select ω as the average over all of the possible γ's, which can be computed as

$$\omega = \int_0^1 [(1-\gamma)^2 + \gamma^2] d\gamma = \frac{2}{3}. \tag{30}$$

Finally, substitution of $a = \frac{1}{2}$ and $\omega = \frac{2}{3}$ into Eqs. (17) and (24), we obtain the variances $c(x_c)$ of the backprojection images on the chords for the parallel-beam and fan-beam projections, respectively, as

$$c(x_c) = \frac{1}{3} \int_{-\frac{\pi}{2}}^{\frac{\pi}{2}} ds\, \sigma^2(u_d, s), \tag{31}$$

$$c(x_c) = \frac{1}{3} \int_{s_a}^{s_b} ds\, \frac{A^2(u_d)}{|\vec{r} - \vec{r}_0(s)|^4} \left| \frac{d\vec{r}_0(s)}{ds} \right|^2 \sigma^2(u_d, s). \tag{32}$$

3.1.5 Noise property of the weighted Hilbert transform over a finite interval

The weighted Hilbert transform constitutes an important step in the chord-based BPF, MDFBP, and FBP algorithms. Consequently, the noise properties of these algorithms depend upon that of the weighted Hilbert transform, which we study below. Let $\hat{f}(x_c, s_a, s_b)$ denote the weighted Hilbert transform of the backprojection image $g(x_c, s_a, s_b)$:

$$\hat{f}(x_c, s_a, s_b) = \frac{1}{b(x_c)} \int_{x_A}^{x_B} \frac{dx'_c}{x_c - x'_c}\, b(x'_c)\, g(x'_c, s_a, s_b). \tag{33}$$

We assume that $g(x'_c, s_a, s_b)$ is band-limited to ν_m. Therefore, the Hilbert transform kernel $\frac{1}{x_c}$ can be replaced by

$$h(x_c) = -\pi j \int_{-\nu_m}^{\nu_m} d\nu\, \text{sgn}[\nu] \mathrm{e}^{2\pi j \nu x_c} = \frac{2\sin^2(\pi \nu_m x_c)}{x_c}. \tag{34}$$

In the presence of noise, the weighted Hilbert transform $\hat{\mathbf{f}}(x_c, s_a, s_b)$ should be interpreted as a stochastic process, which is denoted in boldface. The variance of $\hat{\mathbf{f}}(x_c, s_a, s_b)$ can be written as

$$\begin{aligned} \text{Var}\{\hat{\mathbf{f}}(x_c, s_a, s_b)\} &= \frac{1}{b^2(x_c)} \int_{x_A}^{x_B} dx'_c \int_{x_A}^{x_B} dx''_c\, b(x'_c)\, b(x''_c) \\ &\times\ h(x_c - x'_c)\, h(x_c - x''_c)\, \text{Cov}\{\mathbf{g}(x'_c, s_a, s_b), \mathbf{g}(x''_c, s_a, s_b)\}. \end{aligned} \tag{35}$$

As Eqs. (16) and (23) show, the backprojection image $\mathbf{g}(x_c, s_a, s_b)$ can be treated as an approximated uncorrelated stochastic process. Using the result in Eq. (16) or (23), we can write Eq. (35) as

$$\text{Var}\{\hat{\mathbf{f}}(x_c, s_a, s_b)\} = \frac{1}{b^2(x_c)} \int_{x_A}^{x_B} dx'_c\, c(x'_c)\, h^2(x_c - x'_c)\, b^2(x'_c). \tag{36}$$

In our numerical studies in Secs. 3.2.1 and 3.3.1, we have used $\nu_m = \frac{1}{2\Delta_c}$, where Δ_c denote the sample interval of $\mathbf{g}(x_c, s_a, s_b)$.

3.1.6 Noise properties of chord images

Using Eq. (4), one can write the variance of the reconstructed chord image as

$$\begin{aligned} \text{Var}\{\mathbf{f}_c(x_c, s_a, s_b)\} &\approx \text{Var}\{\hat{\mathbf{f}}(x_c, s_a, s_b)\} \\ &+ \frac{\text{Var}\{\mathbf{P}(u_{d0}, v_{d0}, s_a)\}}{4\pi^2 b^2(x_c)} \left[\frac{\sqrt{(l - x_B)(x_A + l)}}{l - x_c} + \frac{\sqrt{(l + x_A)(l + x_B)}}{l + x_c} \right]^2. \end{aligned} \tag{37}$$

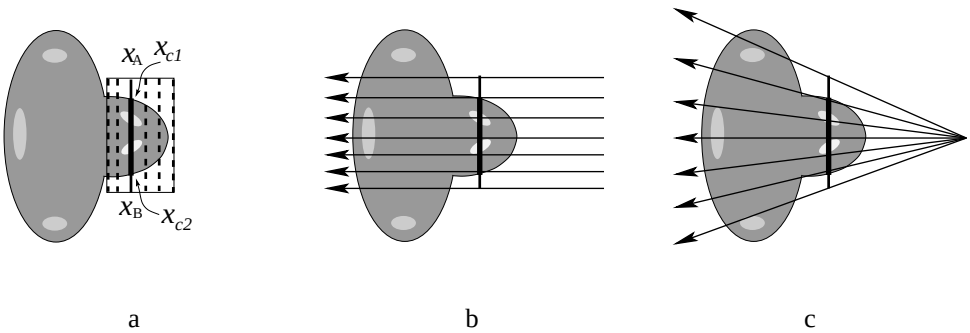

Figure 1: (a) Phantom in the numerical studies. (b) Parallel-beam configuration. (c) Fan-beam configuration. The solid line segment with the endpoints x_A and x_B represents the reconstruction segment. The thick segment with endpoints x_{c1} and x_{c2} indicate the support segment. It should be noted that $[x_A, x_B] \supseteq [x_{c1}, x_{c2}]$. The rectangular ROI is decomposed into a set of (dashed) line segments.

	Circular parallel-beam scan	Circular fan-beam scan	Helical cone-beam scan
Number of views per turn	1024	512	300
Angular range	$[-\frac{\pi}{2}, \frac{\pi}{2}]$	$[-\pi, \pi]$	$[-\pi, \pi]$
Detector bins	256	256	128×128
Detector bin size (mm)	1.1	1.6	3.1×3.1
SDD (mm)	-	200	200
SID (mm)	-	200	200
Helical pitch (mm)	-	-	90

Table 1: Parameters for circular parallel-beam, circular fan-beam, and helical cone-beam scanning configurations which are used in our simulation studies. SDD is the source-to-detector distance and SID denotes the source-to-isocenter distance.

Substituting Eq. (36) into Eq. (37) yields

$$\begin{aligned} \mathrm{Var}\{\mathbf{f}_c(x_c, s_a, s_b)\} &\approx \frac{1}{b^2(x_c)} \int_{x_A}^{x_B} dx'_c \, c(x'_c) \, h^2(x_c - x'_c) \, b^2(x'_c) \\ &+ \frac{\mathrm{Var}\{\mathbf{P}(u_{d0}, v_{d0}, s_a)\}}{4\pi^2 b^2(x_c)} \left[\frac{\sqrt{(l - x_B)(x_A + l)}}{l - x_c} + \frac{\sqrt{(l + x_A)(l + x_B)}}{l + x_c} \right]^2 , \end{aligned} \tag{38}$$

which provides a formula for computing the chord-image variance.

3.2 Numerical studies of noise properties in parallel-beam reconstruction

Using the parallel-beam configuration in Fig. 1b and the parameters given in Table 1, we calculated noiseless projections for the numerical phantom in Fig. 1a. We have used an object-independent Gaussian noise model and an object-dependent Poisson-noise model in the numerical studies. For each noise model, we generated 10,000 sets of noisy data by using noiseless data as the means. The standard deviation σ_0 of Gaussian noise used is 1.6% of the maximum value in the noiseless data, whereas the standard deviation for the Poisson noise is the noiseless data scaled to yield a total photon count of 5×10^5 for each view. We investigated four reconstruction segments with different lengths $L_{AB} = |x_B - x_A|$: 7.8 cm, 10.0 cm, 14.1 cm, and 20.0 cm, all of which are located at $x = 4.06$ cm. It can be observed in Fig. 1b that the length of the support segment, 5.5 cm in length, is shorter than the four reconstruction segments considered. Therefore, the image on this chord can be reconstructed exactly by use of data determined by these reconstruction segments. One can also conclude from Fig. 1b that the minimum data required by the first three reconstruction segments, which are shorter than the maximum dimension (about 15.6 cm) of the object support, are truncated.

3.2.1 Noise properties in reconstruction from truncated parallel-beam data

From the 10,000 sets of data containing Gaussian noise, we used Eqs. (4), (5), and (6) to reconstruct 10,000 noisy $\mathbf{f}_c(x_c, s_a, s_b)$, $\hat{\mathbf{f}}(x_c, s_a, s_b)$, and $\mathbf{g}(x_c, s_a, s_b)$, respectively, on the four reconstruction segments described above. Based upon these noisy reconstructions, we subsequently computed their corresponding empirical variances, which are shown in the upper row of Fig. 2. We compare the empirical results to the analytical results obtained by use of Eqs. (16), (36) and (38). The function $c(x_c)$ is determined by using $\sigma(u_d, s) = \sigma_0$ in Eq. (31), where σ_0 is 1.6% of the maximum value in noiseless data. The analytical results are displayed in the lower row of Fig. 2. Similarly, using Eqs. (4), (5), and (6), we reconstructed 10,000 sets of noisy $\mathbf{g}(x_c, s_a, s_b)$, $\hat{\mathbf{f}}(x_c, s_a, s_b)$, and $\mathbf{f}_c(x_c, s_a, s_b)$ on the four segments from 10,000 sets of data containing Poisson noise. The computed empirical variances from these noisy images are displayed in the upper row of Fig. 3. Using the noiseless data as the Poisson-noise variance $\sigma^2(u_d, s)$ in Eq. (17), one can readily determine $c(x_c)$; and using the determined $c(x_c)$ in Eqs. (16), (36) and (38), one can compute analytical image variances, which are displayed in the lower row of Fig. 3. The results show that the analytical and empirical results agree well with each other, suggesting that Eq. (38) provides an adequate estimation of the chord-image variance.

It can also be observed in Figs. 2c and 3c that, the shorter the reconstruction segment, the higher the chord-image variances. This is only because the second term in (38) increases as L_{AB} (i.e., $(x_A - x_c)(x_c - x_B)$) decreases. However, the difference of the chord-image variances in the central part of the support segment is quite small among these reconstruction segments. The implication of this result is that there may be a significant gain in terms of dose reduction by using a short reconstruction segment, because data required to reconstruct an image on this reconstruction segment is less than that required by using a longer reconstruction segment, thus resulting in a reduced illumination coverage to the object. For similar x-ray intensities, which is directly related to the data-noise level, the reconstruction using a short reconstruction segment appears to yield image variance within the support segment that is comparable to that obtained with a longer reconstruction segment.

We have also performed numerical studies of the noise properties of the reconstructed ROI-images by use of the BPF and MDFBP algorithms from truncated data. Using the numerical phantom in Fig. 1 and each of Gaussian- and Poisson-noise models described above, we generated 500 noisy, truncated data sets for image reconstruction on reconstruction segments of a length L_{AB}=10.0 cm, as shown in Fig. 1a, which completely cover the ROI. We subsequently reconstructed 500 noisy images by using the BPF and MDFBP algorithms. We display in Fig. 4 noisy ROI images reconstructed using the BPF and MDFBP algorithms from data containing Gaussian noise (upper row) and Poisson noise (lower row).

Using the reconstructed 500 sets of Gaussian-noise images and 500 sets of Poisson-noise images, we computed empirical variances of the ROI images, which are shown in the upper row and lower row of Fig. 5, respectively. We display in the third column of Fig. 5 the variance profiles on the dashed lines indicated in the variance images. Results in Fig. 5 support the conclusion that both BPF and MDFBP algorithms yield images with comparable variance levels.

3.2.2 Noise properties in reconstruction from non-truncated parallel-beam data

As discussed above, the FBP algorithm cannot reconstruct exactly images from truncated data. Therefore, we study below the noise properties of the FBP algorithm from parallel-beam data without truncations. For the purpose of comparison, we have also included reconstruction results of the BPF and MDFBP algorithms from the same non-truncated data. Using the numerical phantom in Fig. 1 and each of the Gaussian- and Poisson-noise models, we generated 500 noisy data sets from which 500 noisy images were obtained by use of each of the BPF, MDFBP, and FBP algorithms. Using these noisy images, we computed empirical variance images, which are shown in the upper and lower rows of Fig. 6, respectively, for the Gaussian- and Poisson-noise models. We also display in Fig. 7 the variance profiles on the dashed lines (i.e., on a chord) indicated on the variance images in Fig. 6. The profile results were obtained by use of the BPF (solid), MDFBP (dashed), and FBP (dotted)

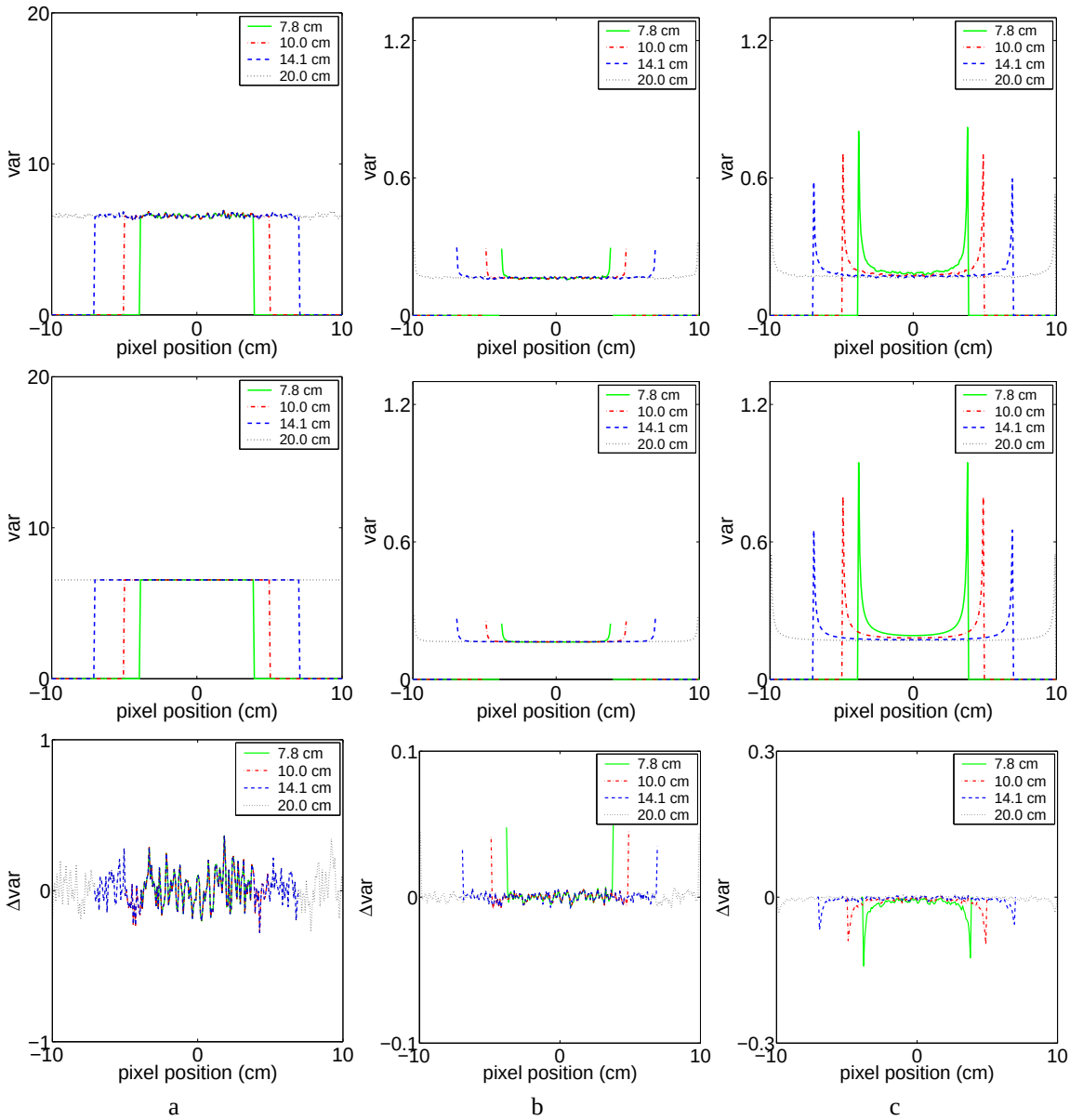

Figure 2: Empirical (top row) and analytical (middle row) variances of (a) $\mathbf{g}(x_c, s_a, s_b)$, (b) $\hat{\mathbf{f}}(x_c, s_a, s_b)$, and (c) $\mathbf{f}_c(x_c, s_a, s_b)$ obtained on four reconstruction segments from parallel-beam data containing Gaussian noise. The difference between empirical variances and analytical variances is also shown in the bottom row, which demonstrates the analytical variances agree well with the empirical variances. The lengths of these segments are indicated in the box in upper-right corners of the plots.

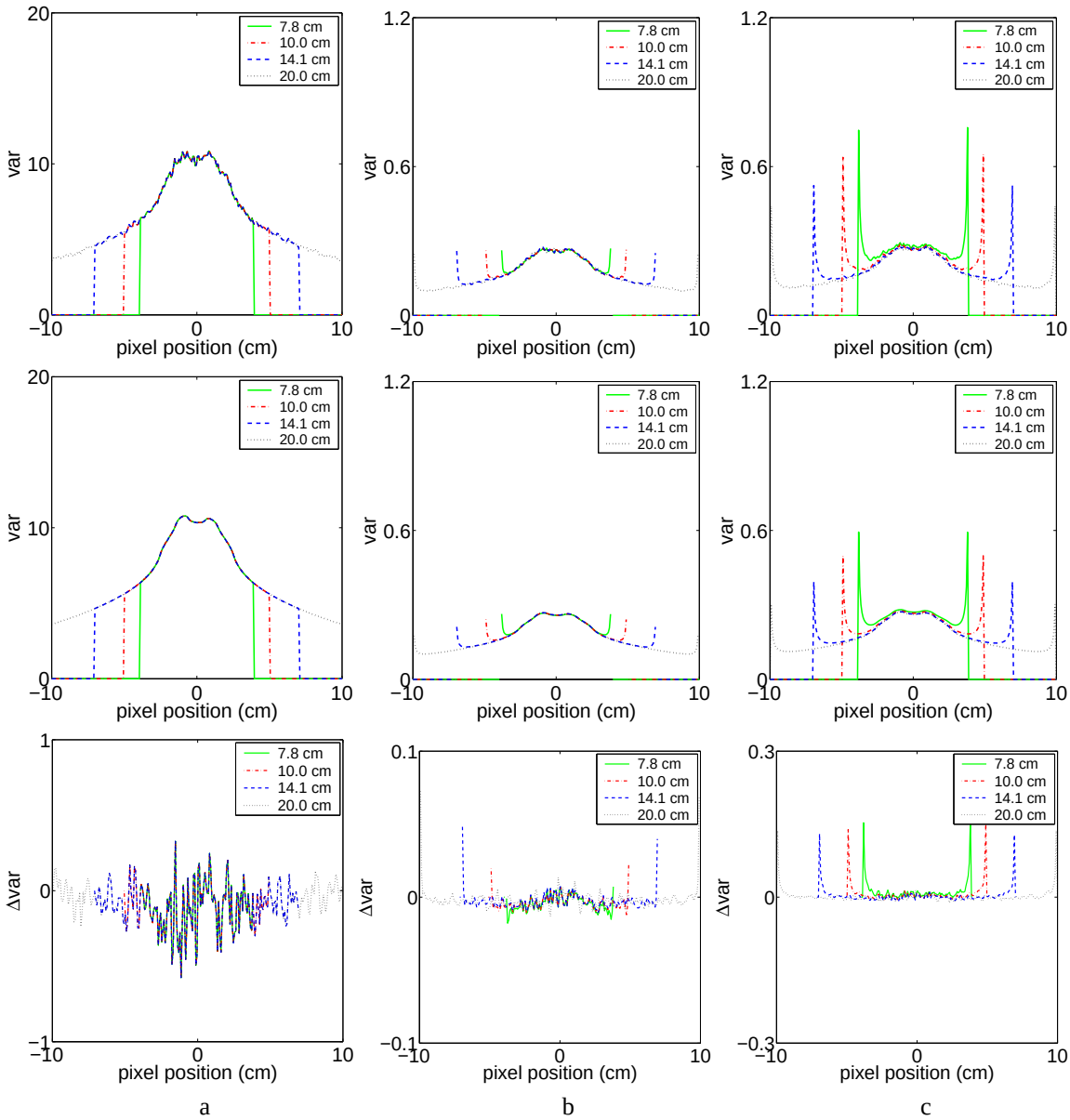

Figure 3: Empirical (top row) and analytical (middle row) variances of (a) $\mathbf{g}(x_c, s_a, s_b)$, (b) $\hat{\mathbf{f}}(x_c, s_a, s_b)$, and (c) $\mathbf{f}_c(x_c, s_a, s_b)$ obtained on four reconstruction segments from parallel-beam data containing Poisson noise. The difference between empirical variances and analytical variances is also shown in the bottom row, which demonstrates the analytical variances agree well with the empirical variances. The lengths of these segments are indicated in the box in upper-right corners of the plots.

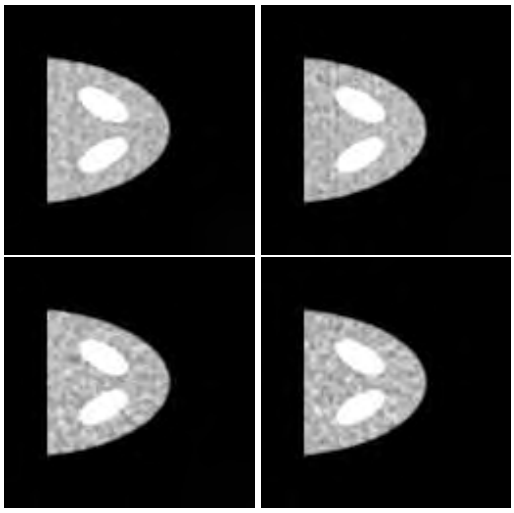

a b

Figure 4: ROI-images obtained by use of the BPF algorithm (a) and MDFBP algorithm (b) from truncated parallel-beam data containing Gaussian noise (upper row) and Poisson noise (lower row).

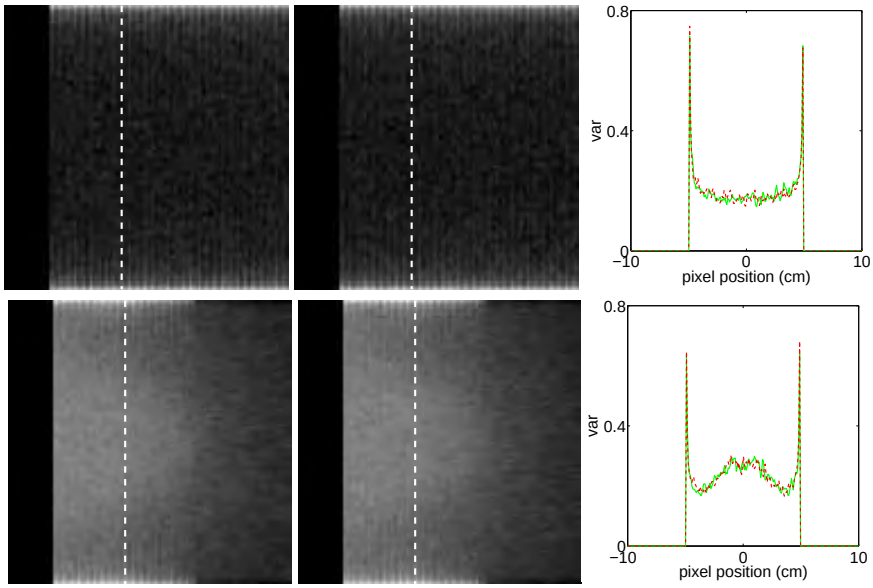

a b c

Figure 5: Empirical ROI-image variances obtained by use of the BPF (a) and MDFBP (b) algorithms from truncated parallel-beam data containing Gaussian noise (upper row) and Poisson noise (lower row), respectively. (c) Variance profiles on the dashed lines indicated in columns (a) and (b) obtained with the BPF (solid) and MDFBP (dashed) algorithms, respectively. For the purpose of displaying the details in the central (i.e., low variance) regions, we have applied a logarithmic scale to the variance images. The display windows are [-0.86, 0.50] and [-1.28, 0.20] for Gaussian noise and Poisson noise, respectively.

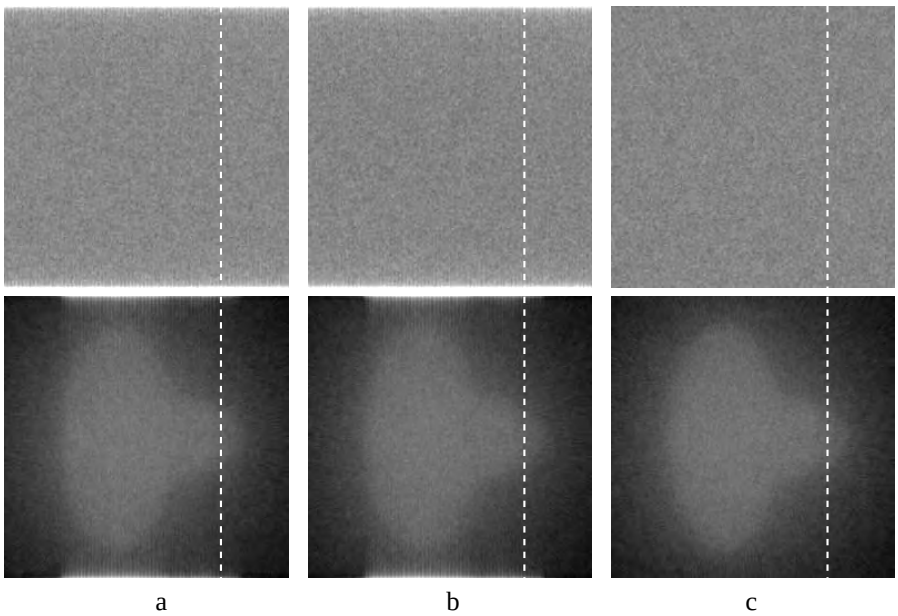

Figure 6: Empirical variance images obtained by use of the BPF (a), MDFBP (b), and FBP (c) algorithms from non-truncated parallel-beam data containing Gaussian noise (upper row) and Poisson noise (lower row). For the purpose of displaying the details in the central (i.e., low variance) regions, we have applied a logarithmic scale to the variance images. The display windows are [-1.3, 0.30] and [-1.3, 0.40] for Gaussian noise and Poisson noise, respectively.

algorithms for the Gaussian-noise model (a) and Poisson-noise model (b). It can be observed that image variances obtained with the three algorithms are similar and that the only difference comes at the extreme ends of the shown reconstruction segments. The BPF and MDFBP algorithms show a significant increase in the image variance at both ends of the profile. The reason for this is that the reconstruction segment was taken to be the width of the image array, and the pre-factor for the finite Hilbert transform in Eqs. (4) and (7) has a singularity at the ends of the reconstruction segment. In practical situations this pre-factor is of little consequence because the reconstruction segment can be selected larger to avoid the singular behavior; furthermore, because the singularity goes as the -1/2 power, its effect is evident only very close to the endpoints of the reconstruction segment.

3.3 Numerical studies of noise properties in fan-beam reconstruction

Using the fan-beam configuration in Fig. 1c and the parameters listed in Table 1, we calculated fan-beam, noiseless data for the numerical phantom in Fig. 1a. We have also used an object-independent Gaussian-noise model and an object-dependent Poisson-noise model in this numerical study. The standard deviation σ_0 of Gaussian noise used is 2.3% of the maximum value in noiseless fan-beam data, whereas the standard deviation for the Poisson noise is the noiseless data scaled to yield a total photon count of 5×10^5 for each view. For each noise model, 10,000 sets of noisy data were generated by use of the corresponding noiseless data as the means. We investigated reconstruction segments of four different lengths L_{AB} =7.8 cm, 10.0 cm, 14.1 cm, and 20.0 cm. All of the segments are located at $x = 4.06$ cm. It can be observed in Fig. 1c that the length of the support segment is 5.5 cm, which is shorter than the four reconstruction segments. Therefore, the image on this chord can be reconstructed exactly by use of data determined by these reconstruction segments. One can also conclude from Fig. 1c that data determined by the first three reconstruction segments, which are shorter than the maximum dimension (about 15.6 cm) of the object support, are truncated.

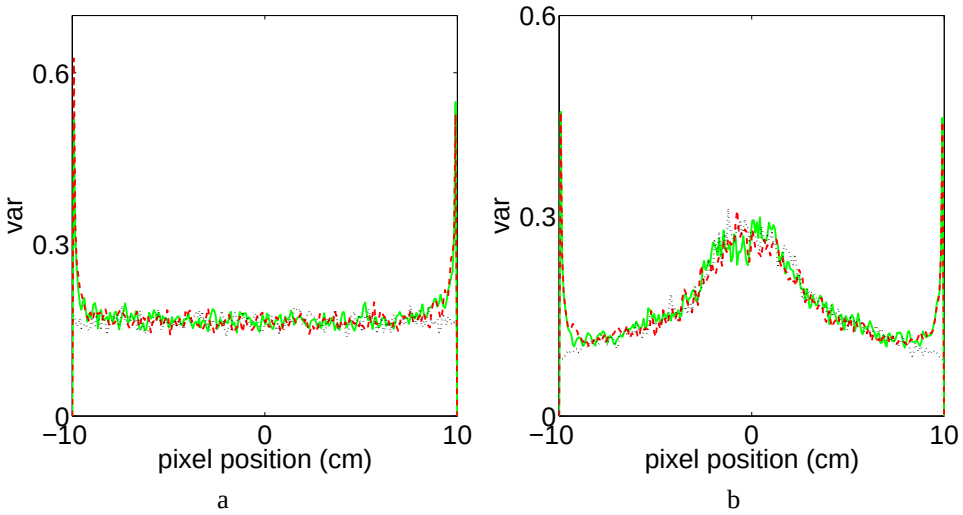

Figure 7: Variance profiles on the dashed lines indicated in variances images shown in Fig. 6. They were obtained for the Gaussian (a) and Poisson (b) noise models by use of the BPF (solid), MDFBP (dashed), and FBP (dotted) algorithms, respectively.

3.3.1 Noise properties in reconstruction from truncated fan-beam data

From the 10,000 sets of data containing Gaussian noise, we used Eqs. (4), (5), and (6) to reconstruct 10,000 noisy $\mathbf{f}_c(x_c, s_a, s_b)$, $\hat{\mathbf{f}}(x_c, s_a, s_b)$, and $\mathbf{g}(x_c, s_a, s_b)$, respectively, on the four reconstruction segments described above. Based upon these noisy reconstructions, we subsequently computed their corresponding empirical variances, which are shown in the upper row of Fig. 8. As for the analytic variance, one can determine $c(x_c)$ by using $\sigma(u_d, s) = \sigma_0$ in Eq. (32), where σ_0 is 2.3% of the maximum value in noiseless fan-beam data. Using $c(x_c)$ in Eqs. (23), (36) and (38), we computed analytically image variances, which are displayed in the lower row of Fig. 8. Similarly, using Eqs. (4), (5), and (6), we reconstructed 10,000 sets of noisy $\mathbf{f}_c(x_c, s_a, s_b)$, $\hat{\mathbf{f}}(x_c, s_a, s_b)$, and $\mathbf{g}(x_c, s_a, s_b)$ on the four segments from 10,000 sets of fan-beam data containing Poisson noise. The computed empirical variances from these noisy images are displayed in the upper row of Fig. 9. Furthermore, using the noiseless fan-beam data as the Poisson-noise variance $\sigma^2(u_d, s)$ in Eq. (32), one can readily determine $c(x_c)$. Using the determined $c(x_c)$ in Eqs. (23), (36) and (38), we computed analytically image variances, which are displayed in the lower row of Fig. 9. It can be observed that the analytic and empirical results agree well with each other, suggesting that Eq. (38) provides an adequate analytic estimation of the chord-image variance for the fan-beam case as well. It is interesting to note in Figs. 8a and 9a that the variances of $\mathbf{g}(x_c, s_a, s_b)$ is spatially varying on the chord. Based upon Eq. (32), one can readily conclude that this spatial variation is caused by the spatially variant factor $\frac{A^2(u_d)}{|\vec{r}-\vec{r}_0(s)|^4}$.

Again, from these results, observations similar to those for the parallel-beam case can be made for the fan-beam case. For example, as Figs. 8c and 9c show, the shorter the reconstruction segment, the higher the chord-image variances. This is only because the second term in (38) increases as L_{AB} (i.e., $(x_A - x_c)(x_c - x_B)$) decreases. The implication of these results is that there may be a significant gain in terms of dose reduction by using a short reconstruction segment, because data required to reconstruct an image on this reconstruction segment is less than that required by using a longer reconstruction segment, which can result in reduction of illumination coverage of the object.

We have also performed numerical studies of the noise properties of the reconstructed ROI-images by use of the BPF and MDFBP algorithms from truncated data. Using the numerical phantom in Fig. 1 and each of the Gaussian- and Poisson-noise models described above, we generated 500 noisy truncated data sets for image reconstruction on reconstruction segments of a length L_{AB}=10.0 cm, as shown in Fig. 1a, which cover the ROI completely. We subsequently reconstruct 500 noisy images by using each of the BPF and MDFBP algorithms.

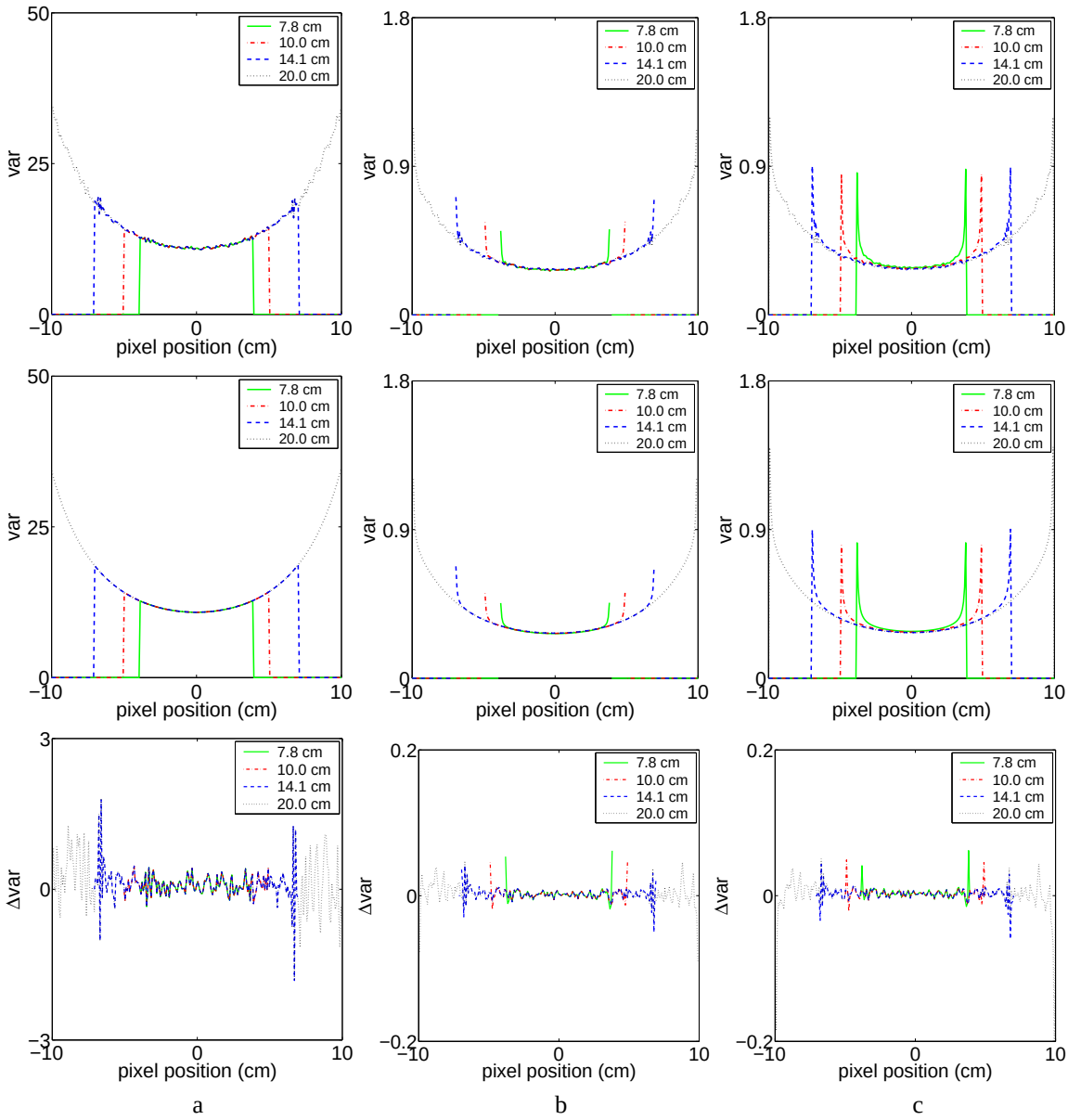

Figure 8: Empirical (top row) and analytical (middle row) variances of (a) $\mathbf{g}(x_c, s_a, s_b)$, (b) $\hat{\mathbf{f}}(x_c, s_a, s_b)$, and (c) $\mathbf{f}_c(x_c, s_a, s_b)$ obtained on four reconstruction segments from fan-beam data containing Gaussian noise. The difference between empirical variances and analytical variances is also shown in the bottom row, which demonstrates the analytical variances agree well with the empirical variances. The lengths of these segments are indicated in the box in upper-right corners of the plots.

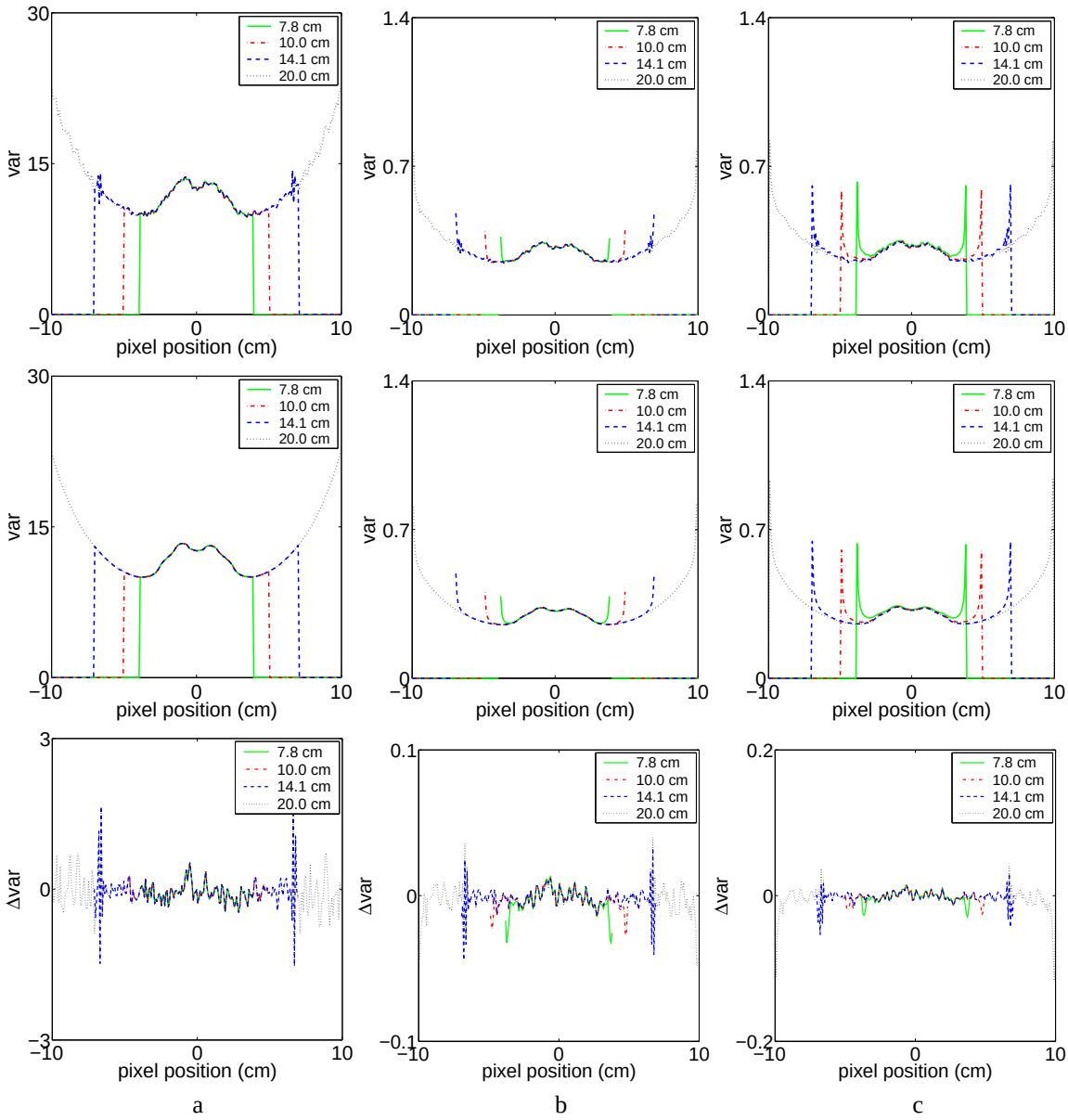

Figure 9: Empirical (top row) and analytical (middle row) variances of (a) $\mathbf{g}(x_c, s_a, s_b)$, (b) $\hat{\mathbf{f}}(x_c, s_a, s_b)$, and (c) $\mathbf{f}_c(x_c, s_a, s_b)$ obtained on four reconstruction segments from fan-beam data containing Poisson noise. The difference between empirical variances and analytical variances is also shown in the bottom row, which demonstrates the analytical variances agree well with the empirical variances. The lengths of these segments are indicated in the box in upper-right corners of the plots.

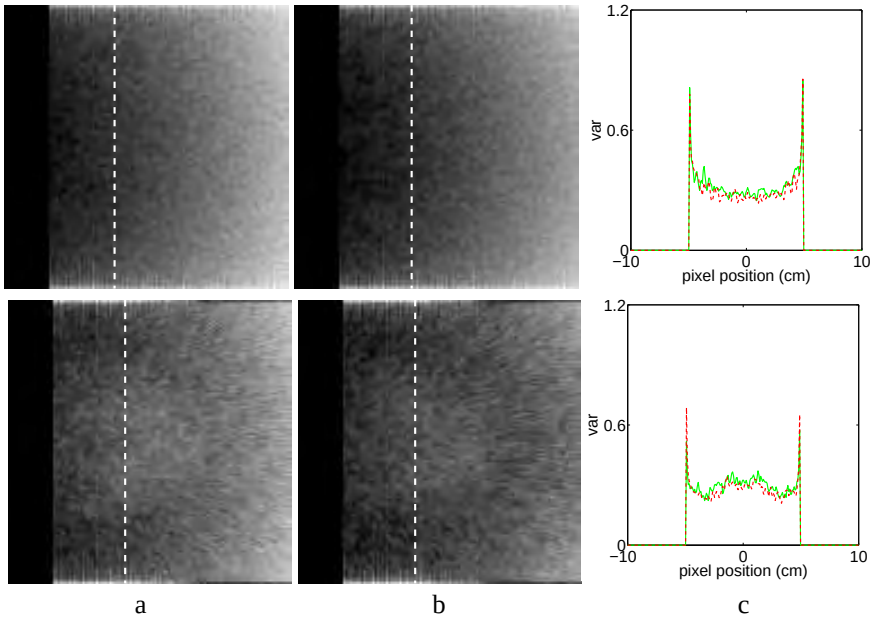

Figure 10: Empirical ROI-image variances obtained by use of the BPF (a) and MDFBP (b) algorithms from truncated fan-beam data containing Gaussian noise (upper row) and Poisson noise (lower row), respectively. (c) Variance profiles on the dashed lines indicated in columns (a) and (b) obtained with the BPF (solid) and MDFBP (dashed) algorithms, respectively. For the purpose of displaying the details in the central (i.e., low variance) regions, we have applied a logarithmic scale to the variance images. The display windows are [-0.76,0.29] and [-0.75,-0.04] for Gaussian noise and Poisson noise, respectively.

Using the reconstructed 500 sets of Gaussian-noise images and 500 sets of Poisson-noise images, we computed empirical variance images within the ROI, which are shown in the upper row and lower row of Fig. 10, respectively. Moreover, we display in the third column of Fig. 10 the variance profiles on the dashed lines indicated in the variance images. Results in Fig. 10 support the conclusion that both BPF and MDFBP algorithms yield images with comparable variance levels.

3.3.2 Noise properties in reconstruction from non-truncated fan-beam data

The FBP algorithm cannot reconstruct exactly images from truncated fan-beam data. Thus, we evaluate below the noise properties of the FBP reconstruction from non-truncated fan-beam data. For the purpose of comparison, we have also included reconstruction results of the BPF and MDFBP algorithms from the same data sets. Using the numerical phantom and fan-beam configuration described above, we generated non-truncated fan-beam data at 512 views uniformly covering 2π. Using the noiseless data as the means, we generated 500 sets of data containing Gaussian noise and 500 sets of data containing Poisson noise. The standard deviation for the Gaussian noise is 2.3% of the maximum value of the noiseless data, whereas the standard deviation for the Poisson noise is the noiseless data scaled to yield a total photon count of 5×10^5 for each view. For a given chord specified by s_a and s_b, one can reconstruct its image from data acquired over the right-side trajectory (i.e., $s \in [s_a, s_b]$), as shown in Fig. 11a. Conversely, one can also reconstruct the chord image from data acquired with both right-side trajectory (i.e., $s \in [s_a, s_b]$) and left-side trajectory (i.e., $s \in [s_b, s_a]$), as shown in Fig. 11b. In chord-based image reconstruction, we decompose image area into chords parallel to the vertical direction, and the source scans from s_a to s_b and then from s_b to s_a, as shown in Fig. 11.

For each chord in the set covering the image area, we first reconstructed the images by use of the BPF, MDFBP, and FBP algorithms from data containing Gaussian noise acquired over the right-side trajectory specified by $s \in [s_a, s_b]$. Subsequently, we computed empirically chord-image variances from these noisy reconstructions. By assembling the chord-image variances, we obtain the variance images, which are shown in the upper row of

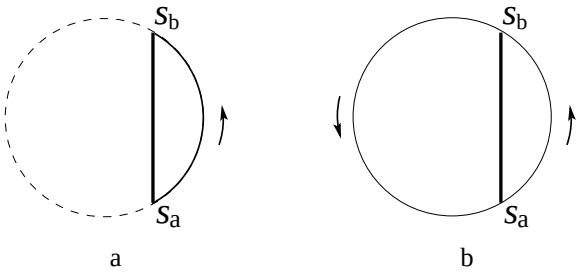

Figure 11: (a) The right-side trajectory (solid) of the chord (thick) specified by s_a and s_b. (b) The right-side trajectory (solid) and left-side trajectory (solid) of the chord (thick) specified by s_a and s_b. The scanning configuration in (b) corresponds to a full, fan-beam scan.

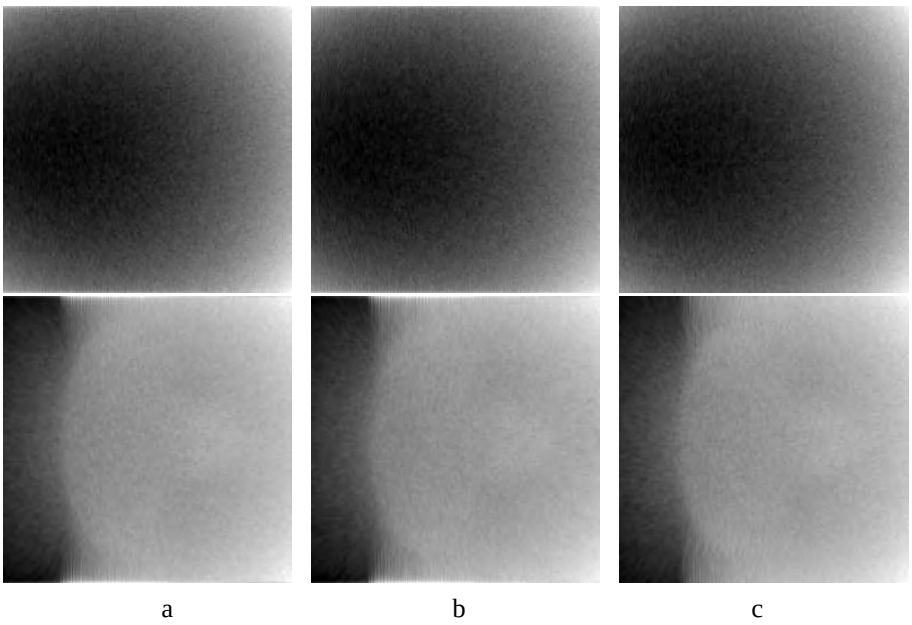

Figure 12: Empirical variance images obtained by use of the BPF (a), MDFBP (b), and FBP (c) algorithms from non-truncated fan-beam data containing Gaussian (upper row) and Poisson (lower row) noise. For the purpose of displaying the details in the central (i.e., low variance) regions, we have applied a logarithmic scale to the variance images. The display window is [-1.0, 0.65] and [-2.02, 0.29] for Gaussian noise and Poisson noise, respectively.

Fig. 12, for the BPF, MDFBP and FBP algorithms, respectively. Similarly, from data containing Poisson noise, we obtained the image variances, which are displayed in lower row of Fig. 12.

We show in column one of Fig. 13 the image variances on a chord specified by $s_a = -\pi/2$ and $s_b = \pi/2$ obtained from data containing Gaussian noise (upper row) and Poisson noise (lower row), respectively. As already seen above, the variance increases as the position along the chord near the source trajectory. There is little difference between the three algorithms. Furthermore, these variance images have similar properties: the chords on the right part have higher and more non-uniform image variance than those on the left part in the image area. In column 2 of Fig. 13, we show the profiles on the middle points across the vertical chords (i.e., on the middle horizontal lines in the variance images shown in Fig. 12). The results reveal that some difference of the MDFBP result from the BPF and FBP results in the peripheral region. This difference may be attributed to the data weighting prior to the backprojection step, which differs from that in the BPF and FBP algorithms. We should point out that this difference is only seen in the extreme periphery of the imaging area. For most practical situations these three algorithms perform virtually identically in terms of image variance.

We investigate further the general trend of the variance decreasing for chords on the left of the variance image. The first impression of this behavior is that this trend is obvious, because the scanning trajectory is on the right

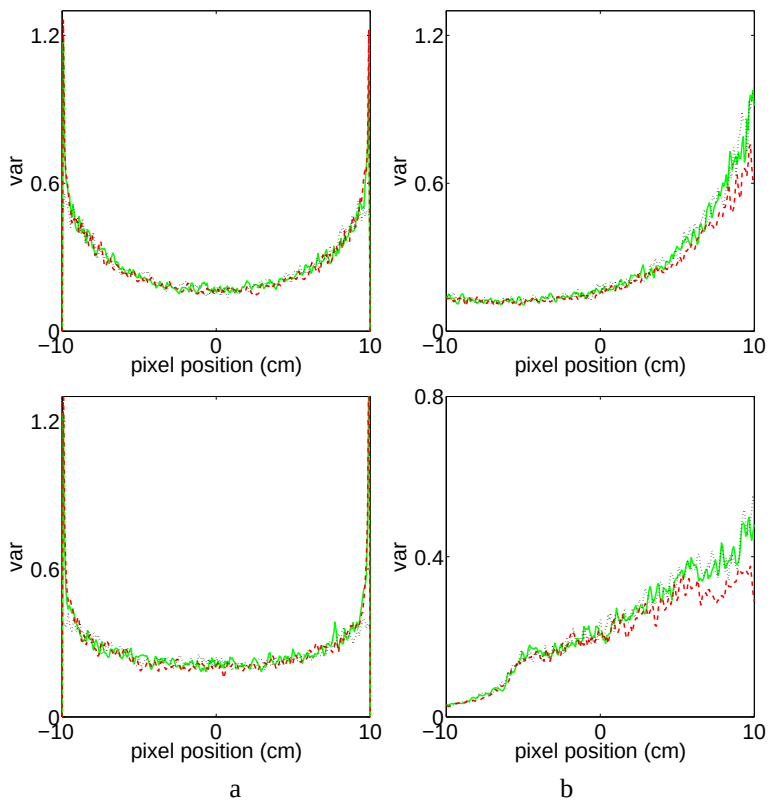

Figure 13: Variance profiles along the central vertical (a) and horizontal (b) lines in variance images shown in Fig. 12, obtained by the BPF (solid), MDFBP (dashed), and FBP (dotted) algorithms from data containing Gaussian noise (upper row) and Poisson noise (lower row).

side, chords on the left of the variance image are reconstructed with a longer scanning trajectory. It appears that more data are used in reconstructing chords covering the left part of the variance image. This explanation is, however, incorrect. First, there is a slight upturn in the variance for the chords on the extreme left of the variance image, which runs counter to this trend. Second, it can be demonstrated that the amount of data going into the chord reconstruction does not necessarily increase as the scanning trajectory increases. Based upon Eq. (32), one can conclude that the true cause of the variance behavior is spatially dependent weighting factor, $1/|\vec{r}-\vec{r}_0(\lambda)|$, in the BPF, MDFBP, and FBP algorithms [19].

For a given chord specified by s_a and s_b, when full scan data are available, one can reconstruct two chord images by use of data acquired with the right-side and left-side trajectories, as shown in Fig. 11 and then obtain a final chord image by averaging the two chord images. We show, in Fig. 14, the variance images of the full scan with accompanying profiles in Fig. 15.

3.4 Numerical studies of noise properties in cone-beam reconstruction

The BPF, MDFBP, and FBP algorithms can yield exact image reconstruction on a chord specified by s_a and s_b as long as the support segment on the chord is illuminated by the x-ray beam at the projection views $s \in [s_a, s_b]$, because these algorithms require data only on the fan-beam projections of the support segment. From the perspective of the chord-based algorithms, the reconstruction of a chord image from cone-beam data is similar to that of a chord image from fan-beam data. In the fan-beam case, the orientation of the fan-beam planes at different views remain unchanged, whereas, in the cone-beam case with a non-planar trajectory, the orientation of the fan-beam-illumination planes generally varies from view to view. As discussed in Sec. 3.1.3, the noise properties of differentiation, backprojection and filtration in the cone-beam case are similar to that in the fan-beam case. Therefore, we include below only the study results on the noise properties of the final chord-images reconstructed

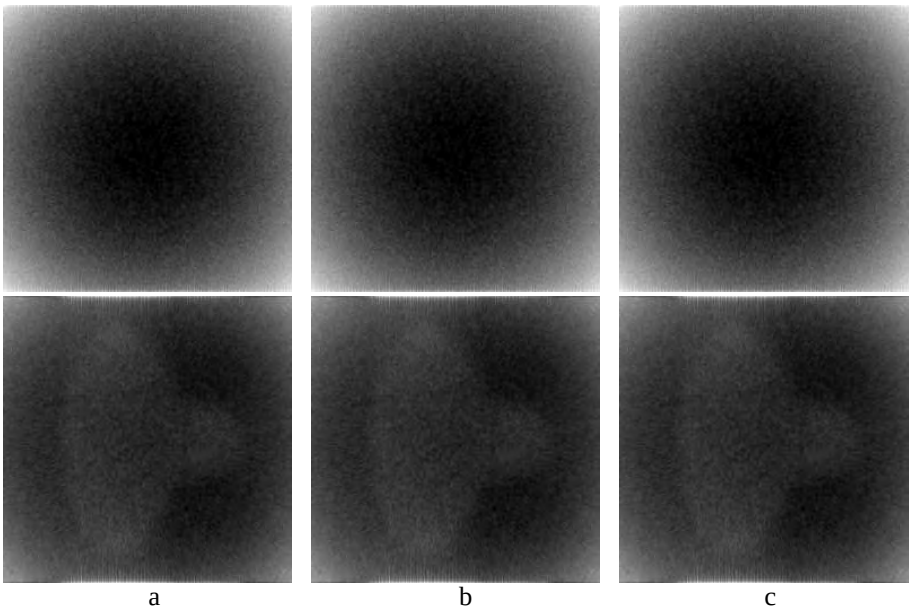

Figure 14: Variance images obtained by use of the BPF (a), MDFBP (b), and FBP (c) algorithms from full-scan fan-beam data containing Gaussian (upper row) and Poisson (lower row) noise. For the purpose of displaying the details in the central (i.e., low variance) regions, we have applied a logarithmic scale to the variance images. The display windows are [-1.19, 0.31] and [-1.18, 0.20] for Gaussian noise and Poisson noise, respectively.

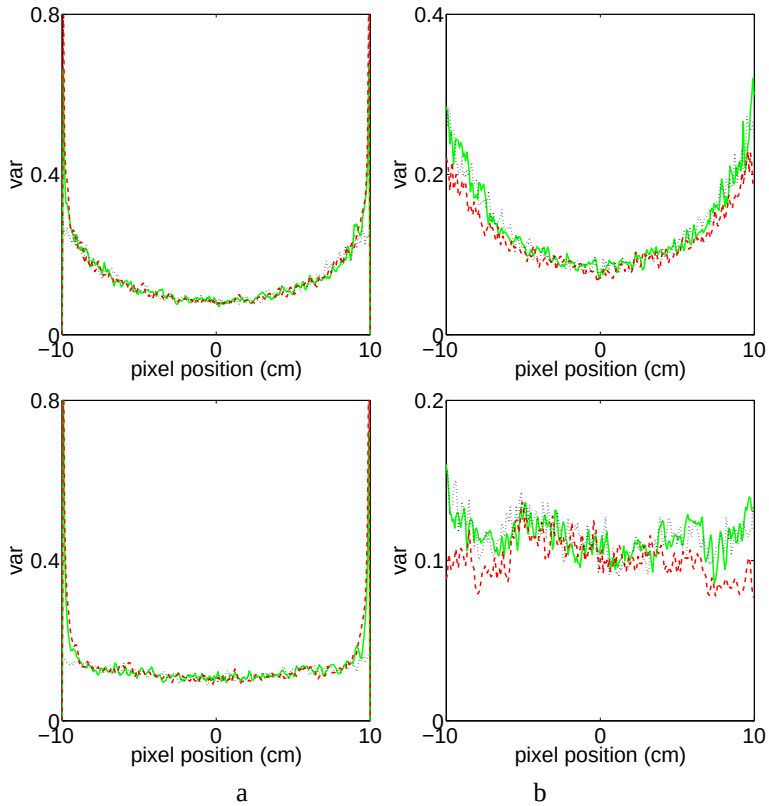

Figure 15: Variance profiles along the central vertical (a) and horizontal (b) lines in variance images, which are shown in Fig. 14, obtained by the BPF (solid), MDFBP (dashed), and FBP (dotted) algorithms from data containing Gaussian noise (upper row) and Poisson noise (lower row).

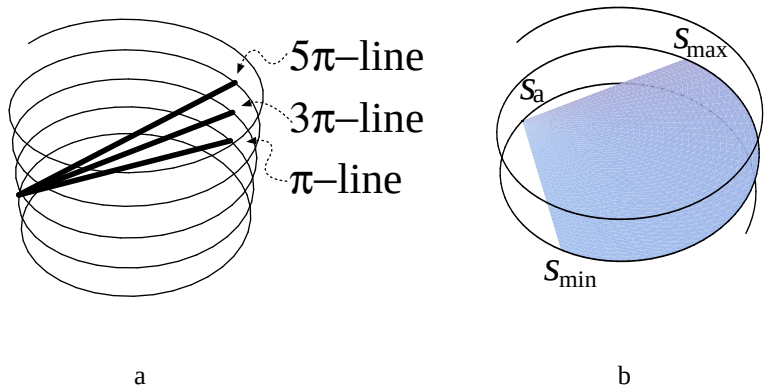

Figure 16: (a) π-line, 3π-line, and 5π-line segments in a helical scan. (b) Surfaces generated in the imaging volume by concatenating π-line segments specified by $s_a = -\pi$ and $s_b \in [-0.5\pi, 0.5\pi]$.

from cone-beam data.

3.4.1 Helical cone-beam configuration

In our investigation of the noise properties of image reconstruction from cone-beam data, we consider the helical trajectory, which is the most widely used in clinical and industrial CT. For a helical scan, the source trajectory is described mathematically as $\vec{r}_0(s) = (R\cos s, R\sin s, \frac{h}{2\pi}s)$, where R is the source to center-of-rotation distance, and h indicates the helical pitch length. For a chord specified by s_a and s_b, if $(n-1)\pi \leq |s_b - s_a| \leq (n+1)\pi$, where n is a positive odd integer, the chord is also referred to as an $n\pi$-line segment [20, 21], as shown in Fig. 16a. In particular, when $n = 1$ and thus $0 \leq |s_b - s_a| \leq 2\pi$, the chord is referred to as a π-line segment [2, 11]. In this work we consider image reconstruction only on π-line segments for the reason that the imaging volume enclosed by the helix can be filled uniquely and completely by π-line segments [11, 12]. Thus, π-line segments can be used to form 3D images in a helical cone-beam scan.

We computed the noiseless data from a Shepp-Logan phantom by use of the configuration parameters in Table 1. Using the noiseless data as the means, we subsequently generated 500 sets of data containing Gaussian noise and 500 sets of data containing Poisson noise, respectively. The standard deviation of Gaussian noise is chosen to be 0.7% of the maximum value of the noiseless data, whereas the standard deviation for the Poisson noise is the noiseless data scaled to yield a total count of 5×10^5 for each view.

3.4.2 Noise properties in reconstruction from helical cone-beam data

A curved surface in the helix volume can be formed by a set of π-line segments for which we fix one end-point at s_a and sweep the other endpoint over a range $s_b \in [s_{\text{min}}, s_{\text{max}}]$. We show in Fig. 16a a curved surface obtained by concatenating a set of π-line segments specified by $s_a = -\pi$ and $s_b \in [-0.5\pi, 0.5\pi]$. Using generated noisy helical cone-beam data, we reconstructed noisy images on the π-line surface by use of the BPF, MDFBP, and FBP algorithms. From these noisy images we subsequently computed empirical image variances on the π-line surface. In Fig. 17, we display the image variances obtained with BPF, MDFBP and FBP algorithms from data containing Gaussian noise and Poisson noise.

We also display in Figs. 18a and b image variances on the π-line segment specified by $s_a = -\pi$ and $s_b = 0$ in the surface, obtained from data containing Gaussian noise and Poisson noise, respectively. The image variances show similar characteristics to that of fan-beam image variances observed in Fig. 13. Namely, the variance image on the π-line surface in Fig. 17 has a structure that is similar to the right-side scan fan-beam results presented in Sec. 3.3.1; the images on π-line segments reconstructed from smaller helix segments tend to have higher and more non-uniform variances. The similarity with the fan-beam case is not surprising because the geometrical

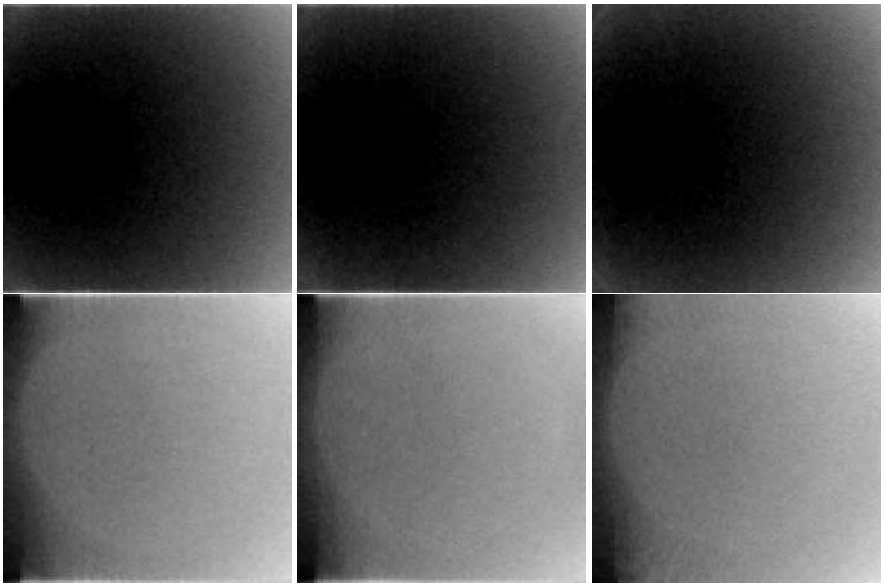

a b c

Figure 17: Empirical variance images on the π-line surface shown in Fig. 16b obtained by use of the BPF (a), MDFBP (b), and FBP (c) algorithms from data containing Gaussian noise (upper row) and Poisson noise (lower row), respectively. For the purpose of displaying the details in the central (i.e., low variance) regions, we have applied a logarithmic scale to the variance images. The display windows are [-1.80, 0.30] and [-1.80, 0.60] for Gaussian noise and Poisson noise, respectively.

arrangement of the π-line with respect to its scanning trajectory is very similar to the relationship between the chords and corresponding fan-beam scanning trajectory. The only difference is that there is an out-of-plane bend to the helix segment.

Regarding the non-uniform shape of the variance, one can attribute the high variance in the image periphery to the weighting factors multiplying the data derivatives before backprojection. As the algorithms are essentially the same for chord-image reconstruction in fan- and cone-beam cases, this conclusion should come as no surprise. In the 2D fan-beam case, the variance non-uniformity and level was reduced by equally weighting reconstructions for both left and right side scans for each chord of the scanning circle. For the helical configuration, it is clear that in a typical scan there will be some overscan for nearly all the chords comprising the volume. But the overscan part of the trajectory does not form a closed loop so using the overscan data to reduce image variance is not as obvious as the case of the circular scan. Future work will focus on how to utilize the overscan data for non-closed trajectories for the purpose of reducing the impact of data noise on chord-base ROI-image reconstruction.

4 Discussion

In this article, we have performed analytic and numerical investigation of the noise properties of chord-based image reconstructions from parallel-, fan-, and cone-beam data. One of the main points of the investigation was to test whether or not the reduced illumination in designing a minimal data set for a particular ROI leads to a significant reduction in exposure. The idea was to compare the statistical properties of the ROI image reconstructed from noise realizations of the minimal data set with noise realizations of the full data set. Similar noise levels were used in both data sets, which are equivalent to modeling similar incident x-ray beam intensities. Our study indicates that the resulting image variance was almost the same for images reconstructed from both data sets. Thus, the minimal data set for ROI reconstruction leads to a significant overall dose reduction, because the body is exposed to lower amount of ionizing radiation in the reduced scan. For fan-beam and cone-beam imaging, we explored the noise properties of the extreme periphery of the imaging region by investigating large fan- and

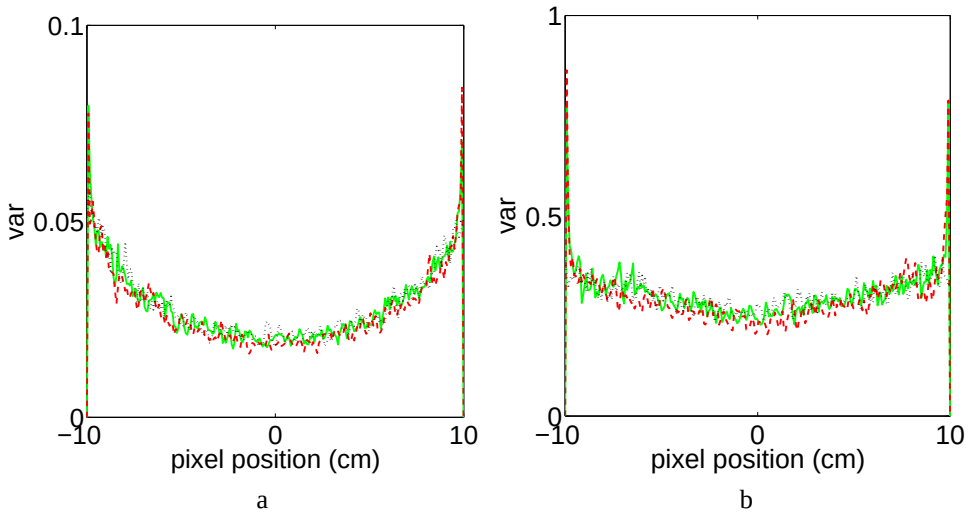

Figure 18: Variances on the central vertical line segment, specified by $s_a = -\pi$ and $s_b = 0$, obtained with the BPF (solid), MDFBP (dashed), and FBP (dotted) algorithms from data containing Gaussian noise (a) and Poisson noise (b).

cone-angles. Image variance non-uniformity was found to be caused by spatially dependent weighting factors in the chord-based reconstruction algorithms. This work represents a study of the noise properties of chord-based reconstruction and of the impact of physical factors on ROI imaging in fan-beam and cone-beam CT. In seeking ways to reduce the impact of noise in volume imaging, we will investigate schemes to incorporate overscan data. The analysis presented in this work can directly be applied to chord-based image reconstruction for general trajectories. Finally, it is important to investigate the behavior of the ROI-reconstruction algorithms when other important factors are included in the data model such as x-ray polychromaticity and non-linear partial volume averaging.

5 Acknowledgments

This work was supported in part by National Institutes of Health grant EB00225 and EB02765. Mr. Dan Xia was supported in part by a DoD Predoctoral training grant BC051553, Dr. Emil Sidky was supported by K01 EB003913, and Mr. Nianming Zuo was supported in part by Natural Science Foundation of China Grant 60328101. Its contents are solely the responsibility of the authors and do not necessarily represent the official views of the National Institutes of Health.

References

[1] A. Katsevich, "Analysis of an exact inversion algorithm for spiral cone-beam CT," *Phys. Med. Biol.*, vol. 47, pp. 2583–2597, 2002.

[2] Y. Zou and X. Pan, "Exact image reconstruction on PI-line from minimum data in helical cone-beam CT," *Phys. Med. Biol.*, vol. 49, pp. 941–959, 2004.

[3] Y. Zou and X. Pan, "An extended data function and its backprojection onto PI-lines in helical cone-beam CT," *Phys. Med. Biol.*, vol. 49, pp. N383–N387, 2004.

[4] E. Y. Sidky, Y. Zou, and X. Pan, "Minimum data image reconstruction algorithms with shift-invariant filtering for helical, cone-beam CT," *Phys. Med. Biol.*, vol. 50, pp. 1643–1657, 2005.

[5] J. D. Pack, F. Noo, and Rolf Clackdoyle, "Cone-beam reconstruction using the backprojection of locally filtered projections," *IEEE Trans. Med. Imaging*, vol. 24, pp. 2317–2336, 2005.

[6] Y. Zou, X. Pan, and E. Y. Sidky, "Theory and algorithms for image reconstruction on chords and within regions of interest," *Journal of the Optical Society of America*, vol. 22, pp. 2372–2384, 2005.

[7] S. Zhao, H. Yu, and G. Wang, "A unified framework for exact cone-beam reconstruction formulas," *Med. Phys.*, vol. 32, pp. 1712–1721, 2005.

[8] T. Zhuang, S. Leng, B. E. Nett, and G. Chen, "Fan-beam and cone-beam image reconstruction via filtering the backprojection image of differentiated projection data," *Phys. Med. Biol.*, vol. 49, pp. 5489–5503, 2004.

[9] J. D. Pack and F. Noo, "Cone-beam reconstruction using 1d filtering along the projection of m-lines," *Inv. Prob.*, vol. 21, pp. 1105–1120, 2005.

[10] Y. Zou and X. Pan, "Image reconstruction on PI-lines by use of filtered backprojection in helical cone-beam CT," *Phys. Med. Biol.*, vol. 49, pp. 2717–2731, 2004.

[11] P. E. Danielsson, P. Edholm, and M. Seger, "Towards exact 3D-reconstruction for helical cone-beam scanning of long objects. a new detector arrangement and a new completeness condition," in *Proceedings of the 1997 International Meeting on Fully Three-Dimensional Image Reconstruction in Radiology and Nuclear Medicine*, D. W. Townsend and P. E. Kinahan, Eds., Pittsburgh, 1997, pp. 141–144.

[12] M. Defrise, F. Noo, and H. Kudo, "A solution to the long-object problem in helical cone-beam tomography," *Phys. Med. Biol.*, vol. 45, pp. 623–643, 2000.

[13] X. Pan, Y. Zou, and D. Xia, "Peripheral and central ROI-image reconstruction from and data-redundancy exploitation in truncated fan-beam data," *Med. Phys.*, vol. 32, pp. 673–684, 2005.

[14] G. Chen, "An alternative derivation of Katsevich's cone-beam reconstruction formula," *Med. Phys.*, vol. 30, pp. 3217–3226, 2003.

[15] F. Noo, M. Defrise, R. Clackdoyle, and H. Kudo, "Image reconstruction from fan-beam projections on less than a short scan," *Phys. Med. Biol.*, vol. 47, pp. 2525–2546, 2002.

[16] Y. Ye and G. Wang, "Filtered backprojection formula for exact image reconstruction from cone-beam data along a general scanning curve," *Med. Phys.*, vol. 32, pp. 654–665, 2005.

[17] X. Pan, D. Xia, Y. Zou, and L. Yu, "A unified analysis of FBP-based algorithms in helical cone-beam and circular cone- and fan-beam scans," *Phys. Med. Biol.*, vol. 49, pp. 4349–4369, 2004.

[18] F. Noo, R. Clackdoyle, and J. Pack, "A two-step Hilbert transform method for 2D image reconstruction," *Phys. Med. Biol.*, vol. 49, pp. 3903–3923, 2004.

[19] X. Pan and L. Yu, "Image reconstruction with shift-variant filtration and its implication for noise and resolution properties in fan-beam computed tomography," *Med. Phys.*, vol. 30, pp. 590–600, 2003.

[20] R. Proksa, T. Köhler, and J. Timmer, "The n-PI-method for helical cone-beam CT," *IEEE Trans. Med. Imaging*, vol. 19, pp. 848–863, 2000.

[21] C. Bontus, T. Köhler, and R. Proksa, "A quasiexact reconstruction algorithm for helical CT using a 3-Pi acquisition," *Med. Phys.*, vol. 30, pp. 2493–2502, 2003.